

# Cross-correlation cosmic shear with the SDSS and VLA FIRST surveys

C. Demetroullas<sup>1\*</sup> & M. L. Brown<sup>1†</sup>

<sup>1</sup>*Jodrell Bank Centre for Astrophysics, School of Physics and Astronomy, The University of Manchester, Manchester, M13 9PL, UK.*

Accepted 2015 XXXXX XX. Received 2015 XXXXX XX; in original form 2015 XXXXX XX

## ABSTRACT

We measure the cosmic shear power spectrum on large angular scales by cross-correlating the shapes of  $\sim 9$  million galaxies measured in the optical SDSS survey with the shapes of  $\sim 2.7 \times 10^5$  radio galaxies measured by the overlapping VLA-FIRST survey. Our measurements span the multipole range  $10 < \ell < 130$ , corresponding to angular scales  $2^\circ < \theta < 20^\circ$ . On these scales, the shear maps from both surveys suffer from significant systematic effects that prohibit a measurement of the shear power spectrum from either survey alone. Conversely, we demonstrate that a power spectrum measured by cross-correlating the two surveys is unbiased, reducing the impact of the systematics by at least an order of magnitude.

We measure an  $E$ -mode power spectrum from the data that is inconsistent with zero signal at the 99% confidence ( $\sim 2.7\sigma$ ) level. The odd-parity  $B$ -mode signal and the  $EB$  cross-correlation are both found to be consistent with zero (within  $1\sigma$ ). These constraints are obtained after a careful error analysis that accounts for uncertainties due to cosmic variance, random galaxy shape noise and shape measurement errors, as well as additional errors associated with the observed large-scale systematic effects in the two surveys. This latter source of uncertainty is particularly important for our analysis as it amplifies the errors by a factor  $\sim 2.5$  compared to the errors due to cosmic variance, galaxy shape noise and measurement errors alone. Our constraints, which probe the power spectrum in the linear régime, are consistent with the expected signal in the concordance cosmological model assuming recent estimates of the cosmological parameters from the *Planck* satellite, and literature values for the median redshifts of the SDSS and FIRST galaxy populations.

The cross-power spectrum approach described in this paper represents a powerful technique for mitigating shear systematics and will be ideal for extracting robust results, with the exquisite control of systematics required, from future cosmic shear surveys with the SKA, LSST, *Euclid* and *WFIRST-AFTA*.

**Key words:** gravitational lensing: weak, methods: statistical, cosmological parameters, galaxies: distances and redshifts

## 1 INTRODUCTION

Gravitational lensing is the apparent distortion in the shapes of distant background galaxies due to the path of their light rays being altered by the gravitational field of a foreground object. In the weak lensing (WL) regime these distortions are so slight that they cannot be measured using only one background source; hence WL is an intrinsically statistical measurement. WL is considered today to be a uniquely powerful tool in astronomy. This is because it can be used to estimate the total mass of a foreground lens regardless of the constituent matter’s fundamental nature.

The tiny coherent WL distortions of background galaxy

shapes caused by the large-scale structure in the Universe is termed cosmic shear. The theoretical basis for cosmic shear was pioneered by [Gunn \(1967\)](#), but due to its challenging observational nature it was only detected around three decades later ([Villumsen 1995](#); [Schneider 1998](#); [Bacon et al. 2000](#); [Kaiser et al. 2000](#); [Van Waerbeke et al. 2000](#); [Wittman et al. 2000](#)). The field has since flourished with numerous experiments delivering results with increasing accuracy ([Van Waerbeke et al. 2001](#); [Brown et al. 2003](#); [Bacon et al. 2003](#); [Fu et al. 2008](#); [Heymans et al. 2012](#); [Jee et al. 2013](#)). Measuring these gravitationally induced distortions at different scales provides a wealth of cosmological information. In particular cosmic shear studies can constrain the clustering amplitude  $\sigma_8$  and the matter density  $\Omega_m$  ([Hoekstra et al. 2006](#); [Schrabback et al. 2010](#); [Kilbinger et al. 2013](#)). Furthermore with forthcoming and future

\* [costantinos.demetroullas@postgrad.manchester.ac.uk](mailto:costantinos.demetroullas@postgrad.manchester.ac.uk)

† [m.l.brown@manchester.ac.uk](mailto:m.l.brown@manchester.ac.uk)

large surveys containing redshift information (e.g. DES<sup>1</sup>, KIDS<sup>2</sup>, HSC<sup>3</sup>, LSST<sup>4</sup>, *WFIRST-AFTA*<sup>5</sup>, *Euclid*<sup>6</sup> and SKA<sup>7</sup>), it will be possible to measure the evolution of the large-scale matter distribution and hence place constraints on the dark energy equation of state  $w$ .

Nearly all cosmic shear studies to date have been performed in the optical and near infrared (NIR). The only comparable study in the radio band is the analysis of the VLA FIRST<sup>8</sup> survey described in [Chang et al. \(2004\)](#). Weak lensing in the radio is still at an early stage compared to lensing at optical/NIR wavelengths. The primary reason for this is the relatively small number of sources in the radio sky at current telescope sensitivities. Current radio surveys can deliver source counts of  $\sim 100 \text{ deg}^{-2}$ , of which  $\sim 25\%$  can be used in weak lensing studies ([Becker et al. 1995](#); [Chang et al. 2004](#)). This can be compared to optical surveys which can reach source number density of  $\sim 10 \text{ arcmin}^{-2}$  over similar area of sky (e.g. [Ahn et al. 2014](#)). This, together with the inability of radio surveys to deliver redshifts for the detected galaxies, means that WL studies in the radio cannot currently compete with state-of-the-art optical/NIR WL experiments.

This situation is expected to change in the foreseeable future. The number counts of radio sources will increase dramatically when radio telescopes breach the  $1\text{--}10 \mu\text{Jy}$  sensitivity level, at which point radio and optical galaxy counts will be comparable. Ongoing and future surveys with the JVLA<sup>9</sup> and e-MERLIN<sup>10</sup> facilities, the SKA pathfinders MeerKAT<sup>11</sup> and ASKAP<sup>12</sup>, and finally the SKA itself, will achieve and ultimately surpass this sensitivity level. Additionally with the advent of the SKA, the detection of radio galaxies will also be accompanied by estimates of their redshifts from measuring their HI emission.

Where galaxy numbers are comparable, radio WL studies provide potential advantages over their optical/NIR counterparts. Radio interferometers have well-known and deterministic beam patterns. Therefore the instrumental point spread function (PSF) can be estimated, at any position on the sky, to very high accuracy. This is in contrast to optical studies where the PSF is typically mapped across the sky using point sources (stars) and is then extrapolated to the positions of the galaxies. This PSF measurement and interpolation scheme will inevitably introduce errors to the subsequent galaxy shape measurements at some level.

Future radio surveys are also expected to be sensitive to the star-forming galaxy population to higher redshifts than is typically probed with optical surveys ([Brown et al. 2013, 2015](#)). Radio WL surveys are therefore expected to probe the Universe at earlier times. Additionally, [Brown & Battye \(2011\)](#) demonstrated the potential use of polarisation information (which comes relatively easy with radio observations) to estimate the orientations of galaxies prior to lensing. This technique can be used to suppress the impact of intrinsic galaxy alignments, a key astrophysical systematic effect that contaminates weak lensing studies at all wavelengths

(see [Joachimi et al. 2015](#), [Kiessling et al. 2015](#) and [Kirk et al. 2015](#) for a recent overview). Radio polarization measurements can potentially also be used to significantly reduce the number of galaxies required for a weak lensing study. Looking to even higher redshifts, [Poursidou & Metcalf \(2014\)](#) have shown that one can exploit 21cm SKA surveys to perform weak lensing studies without having to resolve or even identify individual galaxies. For more details on the SKA WL prospects in general see [Brown et al. \(2015\)](#).

Another key advantage, which we aim to exploit in this paper, arises when radio and optical/NIR data are combined. WL analyses rely on extremely accurate (and, to a lesser extent, precise) measurements of galaxy shapes. However instrumental systematic effects can introduce correlated errors in the measurements. Since it is primarily correlations in the galaxy shapes that one wishes to measure for cosmology, such instrumental systematics represent a significant problem for WL surveys. The source of systematic effects in optical/NIR telescopes and radio interferometers are of a very different origin and nature, and are therefore not expected to correlate. By cross-correlating the shape information from two such experiments, one therefore expects to cancel out any instrumental systematics and obtain an unbiased cosmic shear measurement ([Jarvis & Jain 2008](#); [Patel et al. 2010](#)). In this paper, we aim to demonstrate the potential benefits of such cross-correlation techniques by performing an exploratory optical-radio cross-correlation weak lensing analysis of the VLA FIRST survey ([Becker et al. 1995](#)) and the Sloan Digital Sky Survey (SDSS, [York et al. 2000](#)). These two surveys are well suited for this investigation as they provide approximately  $10,000 \text{ deg}^2$  of overlapping sky coverage. In contrast to most other cosmic shear analyses, our measurements probe the shear power spectrum on large scales, at multipoles  $\ell < 100$ , corresponding to angular scales above a few degrees. We perform our analysis using a cross-power spectrum approach, which provides for a natural decomposition of the signal into its constituent  $E$ - and  $B$ -modes, and also fully accounts for the surveys' masks and geometries on the curved sky.

The paper is organised as follows. In Section 2 we present the relevant weak lensing formalism, and the details of our algorithm for estimating the cosmic shear cross-power spectrum from the data. Section 3 describes the two surveys that we use in the analysis. In Section 4 we describe how we construct shear maps from the two datasets. We identify large-scale systematic effects in these maps which dominate the measured shear auto-correlations in either dataset alone. We demonstrate using simulations in Section 5 that the systematics can be removed by cross-correlating the shape information from the two datasets. In Section 6 we present the results from the analysis of the real data where we measure the shear cross-power spectrum from the FIRST and SDSS datasets. We discuss our results and conclude in Section 7.

## 2 WEAK LENSING THEORY

Distortions in the shapes of distant galaxies can be quantified via measurements of their ellipticity, which is a spin-2 quantity:

$$\epsilon_{ij} = \begin{pmatrix} \epsilon_1 & \epsilon_2 \\ \epsilon_2 & -\epsilon_1 \end{pmatrix}. \quad (1)$$

The two components of this matrix represent the two orthogonal modes of an ellipse:  $\epsilon_1$  describes elongation or compression along or perpendicular to a user-defined reference axis while  $\epsilon_2$  describes elongation or compression at an angle  $\pi/4$  to the reference axis. Galaxy ellipticity can also be described in terms of a semi-major

<sup>1</sup> Dark Energy Survey, <http://www.darkenergysurvey.org>

<sup>2</sup> Kiilo Degree Survey, <http://kids.strw.leidenuniv.nl>

<sup>3</sup> Hyper Suprime-Cam, <http://www.naoj.org/Projects/HSC>

<sup>4</sup> Large Synoptic Survey Telescope, <http://www.lsst.org>

<sup>5</sup> Wide-Field IR Survey Telescope, <http://wfirst.gsfc.nasa.gov>

<sup>6</sup> *Euclid* satellite, <http://sci.esa.int/euclid>

<sup>7</sup> Square Kilometre Array, <http://www.skatelescope.org>

<sup>8</sup> Very Large Array; Faint Images of the Radio Sky at Twenty centimetres

<sup>9</sup> Jansky VLA, <https://science.nrao.edu/facilities/vla>

<sup>10</sup> <http://www.e-merlin.ac.uk>

<sup>11</sup> <http://www.ska.ac.za/meerkat/>

<sup>12</sup> <http://www.atnf.csiro.au/projects/askap/index.html>

axis ( $a$ ), a semi-minor axis ( $b$ ), and a position angle ( $\phi$ ) as

$$\epsilon_1 = \epsilon \cos(2\phi), \quad (2)$$

$$\epsilon_2 = \epsilon \sin(2\phi). \quad (3)$$

Here,  $\epsilon = (a-b)/(a+b)$  is the modulus of the galaxy's ellipticity and  $\phi$  is the position angle of the galaxy with respect to the reference axis of the chosen coordinate system.

In the absence of intrinsic galaxy alignments, galaxy ellipticity is an unbiased estimator for the lensing shear field, which is also a spin-2 quantity,

$$\langle \epsilon_{ij} \rangle = \gamma_{ij} \equiv \begin{pmatrix} \gamma_1 & \gamma_2 \\ \gamma_2 & -\gamma_1 \end{pmatrix}, \quad (4)$$

where the angled brackets denote an ensemble average. Since gravity is a potential theory, the shear at angular position  $\Omega$  can be related to a lensing potential ( $\psi$ ) as

$$\gamma_{ij}(\Omega) = \left( \delta_i \delta_j - \frac{1}{2} \delta_{ij}^K \delta^2 \right) \psi(\Omega), \quad (5)$$

where  $\delta_i \equiv r(\delta_{ij} - \hat{r}_i \hat{r}_j \nabla_i)$  is a dimensionless, transverse differential operator, and  $\delta^2 = \delta_i \delta^i$  is the transverse Laplacian. The lensing potential can in turn be related to the 3-D gravitational potential,  $\Phi(\mathbf{r})$  by (e.g. Kaiser 1998)

$$\psi(\Omega) = \frac{2}{c^2} \int_0^r dr' \left( \frac{r-r'}{rr'} \right) \Phi(\mathbf{r}'), \quad (6)$$

where  $r$  is the comoving distance to the sources.

Note that the ellipticity and shear fields of equations (1)–(4) are defined with respect to an arbitrarily defined reference axis. In the case where one is interested in the weak lensing distortion in a population of background sources due to the presence of a known foreground object (or “lens”), it is more natural to consider the tangential and rotated shear (or ellipticity), defined by

$$\gamma_t = \gamma_1 \cos(2\theta) + \gamma_2 \sin(2\theta), \quad (7)$$

$$\gamma_r = -\gamma_1 \sin(2\theta) + \gamma_2 \cos(2\theta), \quad (8)$$

where  $\theta$  is the position angle formed by moving counter clockwise from the reference axis to the great circle connecting each source-lens pair. The tangential shear,  $\gamma_t$ , describes distortions in a tangential and/or radial direction with respect to the lens position. The rotated shear,  $\gamma_r$ , describes distortions in the orthogonal direction, at an angle  $\pm\pi/4$  to the vector pointing to the lens position.

As indicated by equation (4), the shear components can be estimated by averaging over a set of observed background galaxy ellipticities. The shear field can itself be related to the lensing convergence field (which measures the projected surface mass density contrast) by (Kaiser & Squires 1993)

$$\kappa = \partial^{-2} \partial_i \partial_j \gamma_{ij}, \quad (9)$$

where  $\partial^{-2}$  is the inverse 2-D Laplacian operator defined by

$$\partial^{-2} \equiv \frac{1}{2\pi} \int d^2 \hat{r}' \ln |\hat{r} - \hat{r}'|. \quad (10)$$

A second decomposition of the shear yields the odd-parity divergence field,

$$\beta = \partial^{-2} \epsilon_i^n \partial_j \partial_n \gamma_{ij}, \quad (11)$$

where  $\epsilon_i^n$  is the Levi-Civita symbol in two dimensions,

$$\epsilon_i^n = \begin{pmatrix} 0 & -1 \\ 1 & 0 \end{pmatrix}. \quad (12)$$

Since gravitational lensing produces no  $\beta$ -modes, at least to first order, the divergence field is a useful quantity for testing systematic effects in weak lensing studies.

## 2.1 Weak lensing in spherical harmonic space

As mentioned above, lensing shear is a spin-2 field, i.e. it transforms as  $\gamma \rightarrow \gamma e^{i2\phi}$  under rotation by  $\phi$  (where, for convenience we have defined the complex shear  $\gamma = \gamma_1 + i\gamma_2$ ). One may thus expand  $\gamma$  and its complex conjugate in terms of the spin-weighted spherical harmonics,  ${}_s Y_{\ell m}$  (Newman & Penrose 1966) as

$$\begin{aligned} \gamma(\Omega) &= \gamma_1(\Omega) + i\gamma_2(\Omega) \\ &= \sum_{\ell m} (\kappa_{\ell m} + i\beta_{\ell m}) {}_2 Y_{\ell m}(\Omega), \end{aligned} \quad (13)$$

$$\begin{aligned} \gamma^*(\Omega) &= \gamma_1(\Omega) - i\gamma_2(\Omega) \\ &= \sum_{\ell m} (\kappa_{\ell m} - i\beta_{\ell m}) {}_{-2} Y_{\ell m}(\Omega), \end{aligned} \quad (14)$$

where  $s$  denotes the spin and the summation in  $m$  is over  $-\ell \leq m \leq \ell$ .  $\kappa_{\ell m}$  and  $\beta_{\ell m}$  are the spin-2 harmonic modes of the so-called electric (i.e. “gradient” or “E-mode”) and magnetic (i.e. “curl” or “B-mode”) components of the shear field respectively, which we further identify as the harmonic space versions of the lensing convergence and divergence fields mentioned in the previous section. Using the orthogonality of the spin- $s$  spherical harmonics over the whole sphere,

$$\int d\Omega {}_s Y_{\ell m}(\Omega) {}_s Y_{\ell' m'}^*(\Omega) = \delta_{\ell\ell'} \delta_{mm'}, \quad (15)$$

where the spin states must be equal, the harmonic modes of the  $\kappa$  and  $\beta$  fields can be found directly from the shear field,  $\gamma$ ;

$$\kappa_{\ell m} = \frac{1}{2} \int d\Omega [\gamma(\Omega) {}_2 Y_{\ell m}^*(\Omega) + \gamma^*(\Omega) {}_{-2} Y_{\ell m}^*(\Omega)], \quad (16)$$

$$\beta_{\ell m} = \frac{-i}{2} \int d\Omega [\gamma(\Omega) {}_2 Y_{\ell m}^*(\Omega) - \gamma^*(\Omega) {}_{-2} Y_{\ell m}^*(\Omega)]. \quad (17)$$

Taking the average values over the sphere of products of the harmonic coefficients of the  $\kappa$  and  $\beta$  fields, one can construct three possible power spectra:

$$C_\ell^{\kappa\kappa} = \frac{1}{2\ell+1} \sum_m \kappa_{\ell m} \kappa_{\ell m}^*, \quad (18)$$

$$C_\ell^{\beta\beta} = \frac{1}{2\ell+1} \sum_m \beta_{\ell m} \beta_{\ell m}^*, \quad (19)$$

$$C_\ell^{\kappa\beta} = \frac{1}{2\ell+1} \sum_m \kappa_{\ell m} \beta_{\ell m}^*. \quad (20)$$

The parity invariance of weak lensing suggests that  $C_\ell^{\beta\beta}$  and  $C_\ell^{\kappa\beta}$  should be equal to zero in the absence of systematics. However, systematic effects (both instrumental and astrophysical) can give rise to a non-zero  $C_\ell^{\beta\beta}$ . Finite fields and boundary effects can also lead to leakage of power between the three spectra.

In the limit of weak lensing, the two-point statistical properties of the shear and convergence fields are the same (Blandford et al. 1991) so that  $C_\ell^{\gamma\gamma} = C_\ell^{\kappa\kappa}$ . Finally, we can relate the convergence power spectrum to the 3-D matter power spectrum  $P_\delta(k, r)$  through (e.g. Bartelmann & Schneider 2001)

$$C_\ell^{\kappa(i)\kappa(j)} = \frac{9}{4} \left( \frac{H_0}{c} \right)^4 \Omega_m^2 \int_0^{r_H} dr P_\delta \left( \frac{l}{r}, r \right) \left( \frac{\bar{W}_i(r) \bar{W}_j(r)}{a(r)^2} \right), \quad (21)$$

where we have assumed a flat Universe, and we have now considered the more general case where one measures the cross-correlation signal between two different surveys, here denoted with indices  $i$  and  $j$ . In equation (21),  $H_0$  is the Hubble constant,  $a$  is the scale factor of the Universe,  $r$  is comoving distance,  $r_H$  is the comoving distance to the horizon and  $\Omega_m$  is the matter density. The weighting,  $\bar{W}_i(r)$ , is given in terms of the normalised source distribution for each survey,  $G_i(r)dr = p_i(z)dz$ :

$$\bar{W}_i(r) \equiv \int_r^{r_H} dr' G_i(r') \frac{r' - r}{r'}. \quad (22)$$

## 2.2 Power spectrum estimation on a cut sky

The power spectrum estimators of equations (18)–(20) are only unbiased in the case of full sky coverage and in the absence of noise. However, in the analysis which follows we shall be estimating these power spectra from noisy data covering only a fraction of the sky. In order to correct for the effects of limited sky coverage and noise, we adopt a “pseudo- $C_\ell$ ” analysis, originally developed in the context of CMB polarization observations. We provide a brief summary of the technique here and refer the reader to Brown et al. (2005) for further details.

In the presence of finite sky coverage and/or a mask that excludes certain regions of the sky, one can estimate the so-called pseudo- $C_\ell$ ’s directly from a set of shear maps (using fast spherical harmonic transforms from e.g. the HEALPIX software<sup>13</sup>, Górski et al. 2005) as:

$$\tilde{C}_\ell^{A(i)B(j)} = \frac{1}{2\ell + 1} \sum_m \tilde{A}_{\ell m}(i) \tilde{B}_{\ell m}^*(j), \quad (23)$$

where  $\{A, B\}$  are any of the three possible combinations of  $\kappa$  and  $\beta$  and  $\{i, j\}$  denote the two different surveys as before. In the following sections, we will mostly be interested in taking the cross-power spectra of the FIRST and SDSS datasets, i.e. where  $i$  denotes the FIRST dataset and  $j$  denotes SDSS. When cross-correlating two datasets, there are then in principle two possible  $C_\ell^{\kappa\beta}$  power spectra. For simplicity, we will take the average of these and present a single  $C_\ell^{\kappa\beta}$  cross-power spectrum. In equation (23),  $\tilde{A}_{\ell m}$  and  $\tilde{B}_{\ell m}$  denote the spin-2 spherical harmonic modes (found using equations 16 and 17) of weighted versions of the lensing shear field,

$$\tilde{\gamma}(\Omega) = W(\Omega)\gamma(\Omega), \quad (24)$$

where  $W(\Omega)$  is an arbitrary weighting function which can be used to exclude certain regions of the sky and/or downweight noisier sky pixels.

Grouping all three power spectra into a single vector,  $\mathbf{C}_\ell = \{C_\ell^{\kappa\kappa}, C_\ell^{\kappa\beta}, C_\ell^{\beta\beta}\}$ , one can show that the pseudo- $C_\ell$ ’s measured from the weighted shear fields are related to the true power spectra on the full sky via

$$\tilde{\mathbf{C}}_\ell = \sum_{\ell'} M_{\ell\ell'} \mathbf{C}_{\ell'}, \quad (25)$$

where we have introduced the coupling matrix,  $M_{\ell\ell'}$ . This coupling matrix fully encodes how the survey geometries and masks (described via the function,  $W(\Omega)$ ) mix modes, both within a single spectrum (e.g.  $C_\ell^{\kappa\kappa} \rightarrow C_{\ell'}^{\kappa\kappa}$ ), and also between spectra (e.g.  $C_\ell^{\kappa\kappa} \rightarrow C_{\ell'}^{\beta\beta}$ ), and it can be calculated exactly for any given set of weighting functions,  $W(\Omega)$ . Specifically, in our case where we are estimating the cross-power spectra between two datasets, we can

calculate the  $M_{\ell\ell'}$  matrix exactly from the pseudo- $C_\ell$  cross-power spectra (estimated using equation 23) of the weighting functions used for the two different surveys,  $W_i(\Omega)$  and  $W_j(\Omega)$ . Further details and explicit formulae for calculating  $M_{\ell\ell'}$  are provided in Brown et al. (2005).

Recovering an estimate of the power spectra on the full sky is then only a matter of inverting equation (25). When calculating auto-power spectra (from a single survey), one also needs to include a correction for the noise bias arising from the intrinsic dispersion in galaxy shapes and measurement errors. For practical reasons, it is often also convenient to estimate the power spectrum in terms of “band powers” which recover the average power across a range of multipoles,  $\Delta\ell$ . Including these features, the power spectrum estimator becomes

$$\hat{P}_b = \sum_{b'} K_{bb'}^{-1} \sum_{\ell} O_{b'\ell} (\tilde{C}_\ell - \langle \tilde{N}_\ell \rangle_{\text{MC}}), \quad (26)$$

where  $\hat{P}_b$  denotes the debiased combined estimator for band powers of the  $C_\ell^{\kappa\kappa}$ ,  $C_\ell^{\kappa\beta}$  and  $C_\ell^{\beta\beta}$  power spectra. In equation (26),  $\tilde{C}_\ell$  are the pseudo- $C_\ell$ ’s measured from the data and  $\langle \tilde{N}_\ell \rangle_{\text{MC}}$  are the noise-only pseudo- $C_\ell$ ’s estimated from a suite of Monte Carlo (MC) simulations which contain realisations of the noise, and also incorporate the effects of the survey masks. Note that, for our cross-power spectrum analysis, the noise is uncorrelated and so the noise subtraction step (subtraction of the  $\langle \tilde{N}_\ell \rangle_{\text{MC}}$  term) is not required, although we have nevertheless implemented it in our analysis pipeline for completeness.

$K_{bb'}$  is the binned coupling matrix, constructed from  $M_{\ell\ell'}$  as

$$K_{bb'} = \sum_{\ell} O_{b\ell} \sum_{\ell'} M_{\ell\ell'} F_{\ell'} Q_{\ell'b'}, \quad (27)$$

where  $O_{b\ell}$  is a binning operator that bins the  $C_\ell$ ’s into band powers and  $Q_{\ell b}$  is the inverse operator which “unfolds” the band powers into individual  $C_\ell$ ’s. The function,  $F_\ell$  describes the smoothing effect on the underlying shear fields due to the fact that the sky maps are pixelized. This function is provided by the HEALPIX software that we use to pixelize the sky and perform the spin spherical harmonic transforms.

The binning operator we choose to use is

$$O_{b\ell} = \begin{cases} \frac{1}{2\pi} \frac{\ell(\ell+1)}{\ell_{\text{low}}^{(b+1)} - \ell_{\text{low}}^{(b)}}, & \text{if } 2 \leq \ell_{\text{low}}^{(b)} \leq \ell < \ell_{\text{low}}^{(b+1)} \\ 0, & \text{otherwise,} \end{cases} \quad (28)$$

where  $\ell_{\text{low}}^{(b)}$  denotes the lower edge of band  $b$ . With this choice, the quantity  $\ell(\ell+1)C_\ell/2\pi$  is approximated as constant within each band power.

## 3 THE SURVEYS

### 3.1 FIRST data

The VLA FIRST survey (Becker et al. 1995) is a 10,575 deg<sup>2</sup> survey of the sky in the declination range  $-10^\circ \leq \delta \leq 70^\circ$ , and right ascension range  $8 \text{ hrs} \leq RA \leq 17 \text{ hrs}$ . Of the survey’s total sky coverage, 8,444 deg<sup>2</sup> are in the north galactic cap and 2,131 deg<sup>2</sup> are in the south. The data were gathered using the VLA at L-band (1.4 GHz), in B-configuration (maximum baseline length of 11.1 km) and in snapshot mode (<5 minutes per observation). The observations were conducted between 1993 and 2011. The coverage for the southern cap is discontinuous due to poor weather and system failures during the 2011 observations.

<sup>13</sup> see <http://healpix.sourceforge.net>



The beam of the telescope at  $\delta > +4^\circ 33'$  can be approximated by a circular Gaussian with a full width at half maximum (FWHM) of  $5.4''$ . Below  $\delta = +4^\circ 33'$  the beam is elliptical with a FWHM of  $6.4'' \times 5.4''$ , with the major axis running north-south. For  $21 \text{ hrs} < RA < 3 \text{ hrs}$  and  $\delta < -2^\circ 30'$  the ellipticity of the beam increases further to  $6.8'' \times 5.4''$ . The survey achieved an RMS noise level of  $\sim 0.15 \text{ mJy}$ , and delivered positions, flux densities and shape information for  $\sim 1$  million radio sources, of which  $\sim 40\%$  are resolved. Shape information was extracted by fitting an elliptical Gaussian model to each source. The FIRST catalogue provides this shape information via a major and minor axis and a position angle (PA) for each object. Note that the FIRST analysis pipeline includes a deconvolution step to remove blurring due to the telescope's PSF. More information regarding the contents of the FIRST catalogue and how it was generated is available from the FIRST website<sup>14</sup>.

Mainly due to the relatively sparse coverage in visibility (or “ $uv$ ”) space – an unavoidable result of the observation strategy – the deconvolution/CLEANING<sup>15</sup> of the FIRST sources was imperfect. The catalogue therefore contains information about the possibility of a detected source being a residual sidelobe of a nearby brighter source. Of the total number of FIRST sources, 76.4% had a probability of being spurious,  $P(S)$ , less than 5%. For 17% of the sources the probability was between 5 and 50%. The remaining 6.5% had more than a 50% chance of being a sidelobe of a nearby bright galaxy. Additional information about the sources was generated by cross-correlating their positions with positions of optical sources from the SDSS and 2-micron All-Sky Survey (2MASS, [Skrutskie et al. 2006](#)) catalogues.

The FIRST data have previously been used to make a detection of cosmic shear in the radio band by extracting source shape information directly from the  $uv$  plane ([Chang et al. 2004](#)). Those authors measured the 2-point correlation function (2PCF) on angular scales,  $1^\circ < \theta < 40^\circ$ . On scales  $1^\circ < \theta < 4^\circ$  the measured  $\beta$ -modes were consistent with zero while a significant signal was detected in the  $\kappa$ -modes at the  $\sim 3\sigma$  level. From their results, [Chang et al. \(2004\)](#) placed a joint constraint on the clustering amplitude,  $\sigma_8$  and the median redshift of the FIRST sources without an optical counterpart,  $z_m$  of  $\sigma_8(z_m/2)^{0.6} \approx 1.0 \pm 0.2$ . Adopting a prior of  $\sigma_8 = 0.9 \pm 0.1$  they obtained the constraint  $z_m = 2.2 \pm 0.9$  (68% CL). This value is consistent with existing models of the radio source luminosity function. The results are encouraging as they show that although radio surveys lack the sensitivity at the moment to compete with optical lensing surveys, they can deliver shape information which, with the proper processing, can be used for weak lensing studies.

For the purposes of this study we acquired the 13JUN05 version of the FIRST catalogue. The [Chang et al. \(2004\)](#) study estimated the median redshift of the entire FIRST sample to be between 0.9 and 1.4 (depending on the model of the radio source luminosity function used). Using the SKA simulated skies ( $S^3$ , [Wilman et al. 2008](#)) – a computer simulation based on more recent data, and designed to model the radio and submillimetre Universe – we estimate the median redshift of the entire FIRST sample to be  $z_m \sim 1.2$ .

### 3.2 SDSS data

The SDSS is an ongoing (since 2000) optical survey of the north and south galactic caps north of declination  $-15^\circ$ , covering  $\sim 14,500 \text{ deg}^2$  of the sky. The survey uses a 2.5 metre telescope located at Apache Point Observatory (APO) in the Sacramento mountains in south New Mexico ([Abazajian et al. 2003](#); [Ahn et al. 2014](#)). In 2008 the experiment entered a new phase called SDSS-III in which new instruments came into operation ([Eisenstein et al. 2011](#)). One of the SDSS-III surveys, the Baryon Oscillation Spectroscopic Survey (BOSS; [Dawson et al. 2013](#)), obtained spectra of  $\sim 1.4$  million luminous red galaxies (LRGs) and  $\sim 0.3$  million quasars which have subsequently been used to place stringent constraints on cosmological models ([Aubourg et al. 2014](#)).

The SDSS data have been used in numerous weak lensing experiments probing different angular scales on the sky. The data have proved particularly useful for galaxy-galaxy lensing (e.g. [Fischer et al. 2000](#); [Mandelbaum et al. 2006](#)) and cluster lensing (e.g. [Mandelbaum et al. 2008](#); [Sheldon et al. 2009](#); [Roza et al. 2010](#)). In terms of cosmic shear measurements, [Lin et al. \(2012\)](#) and [Huff et al. \(2014\)](#) have both exploited the deep observations of SDSS “Stripe 82” to perform cosmic shear analyses. Both of these latter studies detected a significant  $\kappa$ -mode signal on degree scales with  $\beta$ -modes found to be consistent with zero. Derived constraints on  $\Omega_m$  and  $\sigma_8$  were also found to be consistent between these two independent studies.

In this study, we have used the tenth data release (DR10) of SDSS ([Ahn et al. 2014](#)). DR10 delivers photometric information across 5 bands (u, g, r, i, z) for  $\sim 500$  million galaxies and stars (the PHOTO sample), and spectra for  $\sim 2.5$  million of them (hereafter, the SPECTRO sample). The mean magnitude across all PHOTO galaxies and bands is  $\sim 22.5$ . The median magnitude and redshift for the SPECTRO galaxy population is  $\sim 21$  and  $\sim 0.3$  respectively. The SPECTRO sample includes two distinct populations one of which peaks at  $z \approx 0.15$  and the second at  $z \approx 0.5$ . Only a few galaxies in the sample are at redshifts greater than  $\sim 0.7$ . We chose to download all sources from the SDSS DR10 PHOTO sample that were identified in i-band as galaxies with magnitudes  $i_{\text{mag}} < 26$ . For the  $\sim 38.5$  million sources that met the criteria we acquired information about their positions (RA and  $\delta$ ) and multi-band information describing their flux densities, galaxy types, second and fourth moments, the reconstructed PSF at each galaxy position, the galaxy magnitudes and quoted errors, and finally their extinction.

## 4 SHEAR MAPS AND TESTS FOR SYSTEMATICS

Telescope induced effects can severely bias a WL study. Therefore systematics must be accounted for and if possible corrected. In this section, we describe how we construct pixelized maps of the FIRST and SDSS shear fields from the two galaxy catalogues, and we assess the resulting maps for systematic effects.

### 4.1 FIRST analysis

#### 4.1.1 Source selection

A detailed study of the systematic effects in the FIRST survey was performed in [Chang et al. \(2004\)](#). To control systematics, [Chang et al. \(2004\)](#) first performed a series of cuts on the source catalogue in order to remove from the sample those sources whose shapes were most likely to be corrupted due to residual systematic effects. In this analysis, we have applied as many of their source selection

<sup>14</sup> FIRST website: <http://sundog.stsci.edu/index.html>

<sup>15</sup> The CLEAN algorithm ([Högbom 1974](#)) is a standard technique commonly used in radio astronomy to deconvolve images for the effects of a finite PSF. The algorithm models the data as a collection of point sources and, starting with the brightest source, iteratively subtracts (from the  $uv$ -data) the flux associated with each source in order to detect and characterise fainter objects.

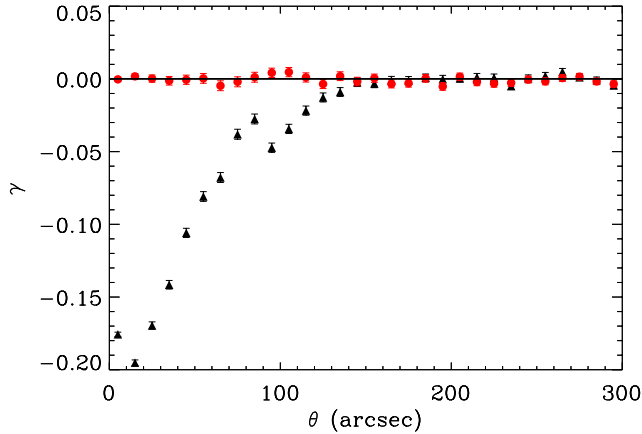


**Figure 1.** Results of the test for residual beam systematics in the FIRST galaxy shapes, as described in Section 4.1.2. A large radial (negative  $\gamma_r$ , black triangles) distortion, decreasing as a function of angular scale,  $\theta$ , is found in the FIRST galaxy ellipticities when their shapes are stacked around the FIRST galaxy positions. The rotated shear ( $\gamma_r$ , red circles) is consistent with zero.

criteria as possible given the information that was available to us in the FIRST catalogue. We therefore discarded sources that had an unresolved deconvolved minor axis, or a deconvolved major axis that was greater than 7 arcsec or smaller than 2 arcsec. We also removed sources that had an integrated flux that was smaller than 1 mJy. Finally we have included only sources that had a possibility of being a sidelobe of a nearby brighter source  $P(S) < 5\%$ . After applying these cuts we were left with  $\sim 2.7 \times 10^5$  radio sources (from an initial sample of  $\sim 1$  million catalogue entries). For all remaining sources, we formed the  $\epsilon_1$  and  $\epsilon_2$  ellipticity estimates from the catalogued major and minor axes, and position angle, according to equations (2) and (3).

#### 4.1.2 Residual systematics in FIRST ellipticities

We have performed a number of quality checks on the data immediately after applying the cuts described above. By far the most informative of these was a test for corruption of the galaxy ellipticities due to residual sidelobe contamination resulting from an imperfect deconvolution and/or CLEANING procedure. To perform this test, we have made use of the g-g lensing tangential and rotated shear constructions ( $\gamma_t$  and  $\gamma_r$ ; equations 7 & 8) and have stacked the shapes of the selected FIRST galaxies around the positions of all of the sources in the original FIRST catalogue (including both resolved and unresolved objects). The results of this test are shown in Fig. 1 where we see a strong distortion in the FIRST galaxy shapes oriented radially from the central stacking position. This signal persists when we randomly choose a sub-set of the FIRST sources' shapes and/or positions. Moreover, the signal shows no obvious dependency on the flux of the stacked and/or central sources.

To further investigate the origin of this signal we repeated the stacking analysis in  $(\Delta RA, \Delta \delta)$  space (i.e. where the positions of all of the central sources are re-mapped to  $\Delta RA = 0; \Delta \delta = 0$ ). The resulting maps of tangential and rotated shear are shown in Fig. 2. The 6-arm star pattern apparent in the  $\gamma_t$  map, displayed in the left panel of Fig. 2, closely matches the synthesised beam (or PSF) of the VLA in “snapshot mode” which was the observation mode employed during collection of the FIRST survey data. The results of

this test clearly indicate the presence of residual systematics in the FIRST galaxy ellipticities, which are strongly correlated with the known PSF of the VLA-FIRST observations. These residuals are clearly spurious, and are almost certainly the result of an imperfect deconvolution and/or CLEANING of the FIRST data during the imaging step in the FIRST data reduction. In the analysis which follows, we will attempt to include the effects of these residual ellipticity correlations by incorporating a model of the systematic in our MC simulations. However, we also expect our cross-power spectrum approach – whereby we cross-correlate the FIRST and SDSS galaxy shapes – to be robust to the presence of this FIRST-specific systematic effect.

#### 4.1.3 FIRST shear maps

The pseudo- $C_\ell$  power spectrum analysis outlined in Section 2.2 requires as input pixelized maps of the shear components. We create these maps by simple averaging of the ellipticities of the FIRST sources which fall within each sky pixel and we use the HEALPIX scheme (Górski et al. 2005) to define the sky pixelisation. We choose the pixel size according to the density of sources in the FIRST survey: with  $\sim 2.7 \times 10^5$  sources surviving the cuts described in Section 4.1.1, a pixel size of  $\sim 1 \text{ deg}^2$  results in a mean pixel occupation number of  $\sim 20$  galaxies. This choice ensures that our maps are contiguous over the survey area and are mostly free from unoccupied pixels within the survey boundaries. We therefore set the HEALPIX resolution parameter,  $N_{\text{side}} = 64$ , which corresponds to a pixel size of  $\sim 0.85 \text{ deg}^2$ .

Fig. 3 shows maps of the shear components,  $\gamma_1$  and  $\gamma_2$ , as reconstructed from the FIRST galaxy ellipticities. These maps are dominated by random noise due to the intrinsic dispersion in galaxy shapes and measurement errors. Visual inspection of the figure does also suggest a weak dependence of the  $\gamma_1$  amplitudes on declination though some of this may simply reflect the varying galaxy number density, which also shows some dependence on declination. (Later in Section 6, we perform a suite of null-tests on our cross-power spectrum results, one of which is to split the datasets according to declination. This test should highlight any significant problems associated with any declination-dependent systematic effects that persist in the FIRST shear maps.)

In addition to the shear maps, we construct a weight map (the  $W(\Omega)$  of equation 24) as simply the number of galaxies that lie within each pixel. In the case of uniform measurement errors on the ellipticities, setting  $W(\Omega)$  to be equal to the galaxy number density is equivalent to an inverse-variance weighting scheme, which, for the noise-dominated régime in which we are working, is the optimal weighting scheme to use. To limit our sensitivity to individual outliers in the galaxy ellipticity distribution, we set  $W(\Omega) = 0$  for pixels that contain less than 5 galaxies. Fig. 4 shows the weight map that results from this process. We use this map to weight the FIRST shear data in the subsequent power spectrum analysis.

## 4.2 SDSS analysis

### 4.2.1 Shape measurements and initial source selection

The SDSS catalogue provides shape information for each detected source as ellipticity components derived from second moments,

$$\epsilon_1 = \frac{Q_{xx} - Q_{yy}}{Q_{xx} + Q_{yy}}, \quad (29)$$

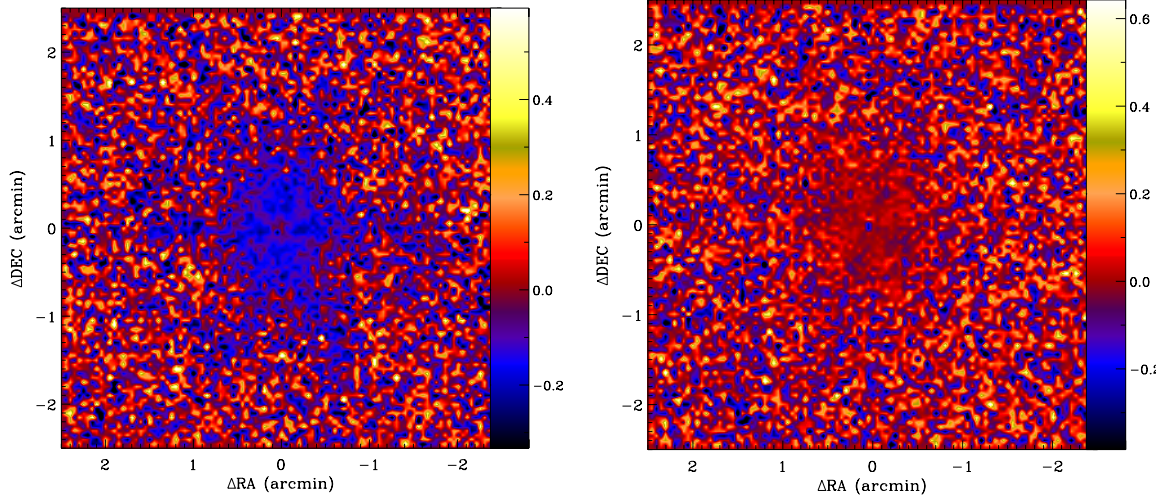


**Figure 2.** Maps of the tangential shear ( $\gamma_t$ , *left panel*) and rotated shear ( $\gamma_r$ , *right panel*) as a function of the separation in RA and  $\delta$  from the central stacking positions. The tangential shear map reveals a negative amplitude 6-arm star pattern which closely resembles the structure in the synthesised beam (PSF) of the VLA snapshot observations.

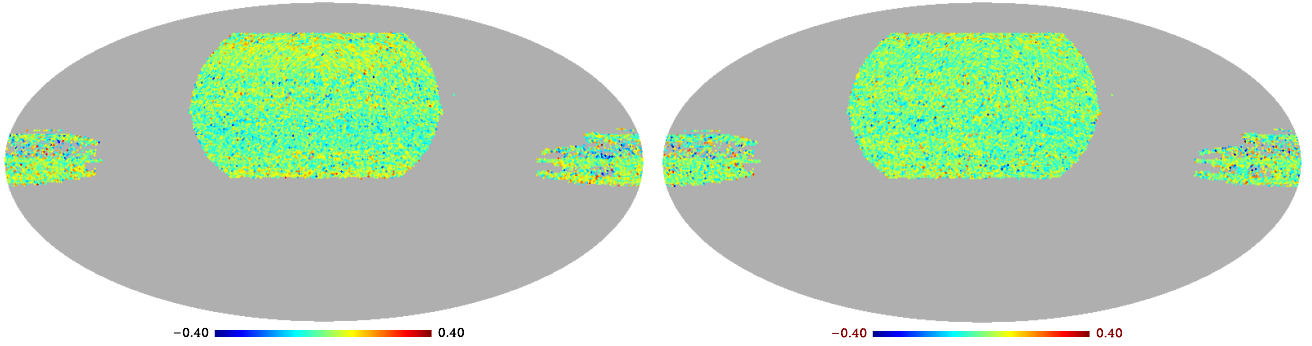


**Figure 3.** Maps of the  $\gamma_1$  (*left panel*) and  $\gamma_2$  (*right panel*) shear components, constructed by simple averaging of the FIRST galaxy ellipticities within each pixel.

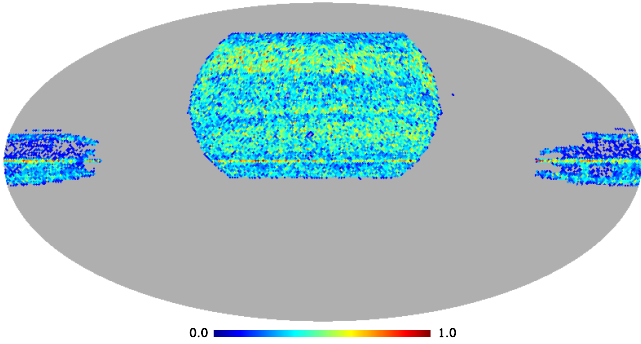


**Figure 4.** The galaxy number density map used to weight the FIRST shear field (Fig. 3) in the power spectrum analysis.

$$\epsilon_2 = \frac{2Q_{xy}}{Q_{xx} + Q_{yy}}, \quad (30)$$

where the adaptive moments are measured directly from the SDSS images according to

$$Q_{ij} = \int d\Omega I(\Omega) w(\Omega) \Omega_i \Omega_j. \quad (31)$$

Here,  $I(\Omega)$  is the object intensity at position  $\Omega = (\Omega_x, \Omega_y)$  and  $\{i, j\}$  can take values  $\{x, x\}$ ,  $\{y, y\}$  or  $\{x, y\}$ . Ideally, adaptive moments are measured using a radial weight function,  $w(\Omega)$ , which is iteratively adapted to the object's size. In practice, the SDSS pipeline used a Gaussian weighting function with a size matched to that of the object being fitted. Such an approach has been shown to be nearly optimal (Bernstein & Jarvis 2002) and is much quicker. The SDSS catalogue's galaxy ellipticities need to be corrected for PSF smearing and atmospheric seeing. To facilitate this, the catalogue also provides moment information that describes the PSF reconstructed at each galaxy's position. We follow the procedure advocated by the SDSS team which corrects the catalogue ellipticities for the effects of seeing and PSF anisotropy according to

$$\begin{aligned} \epsilon_1^{corr} &= (\epsilon_1^{meas} - R\epsilon_1^{psf})/(1 - R) \\ \epsilon_2^{corr} &= (\epsilon_2^{meas} - R\epsilon_2^{psf})/(1 - R), \end{aligned} \quad (32)$$

where  $\epsilon_i^{meas}$  are the galaxy ellipticity components,  $\epsilon_i^{psf}$  are the PSF ellipticity components reconstructed at each galaxy position and  $R$  is a parameter formed from a combination of the second and fourth-order moments of the galaxy and PSF shapes. (For further details, and an explicit formula for  $R$ , see the description on the SDSS



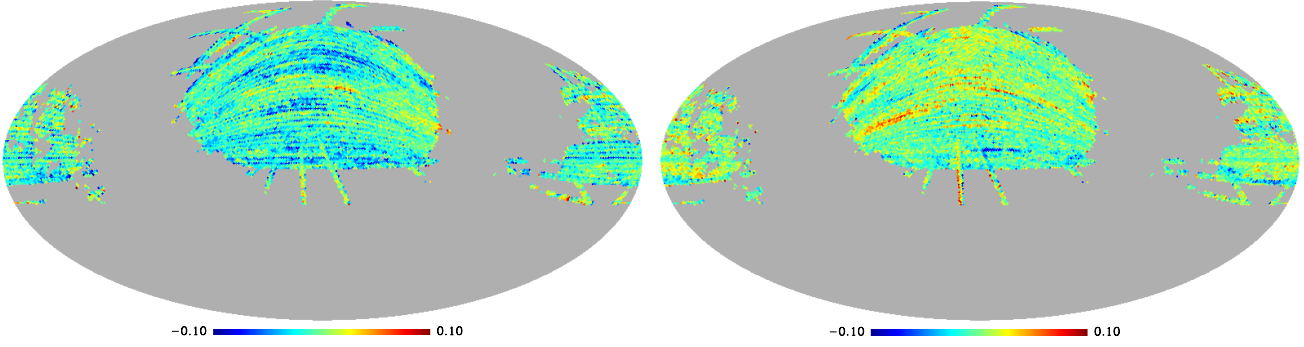


**Figure 5.** Maps of the  $\gamma_1$  (left panel) and  $\gamma_2$  (right panel) shear components, constructed by simple averaging of the SDSS galaxy ellipticities within each pixel. These maps were constructed from the  $\sim 25$  million galaxies remaining in the SDSS shear catalogue immediately after the PSF correction and source selection steps described in Section 4.2.1 were implemented. Significant large-scale systematic effects are clearly evident in these maps.

DR10 catalogue webpage<sup>16</sup>.) As mentioned in the SDSS catalogue description, the correction of equation (32) is not exact and results in a small bias (Bernstein & Jarvis 2002; Hirata & Seljak 2003). However, rather than implementing a more sophisticated correction algorithm, we will mostly appeal to the cross-correlation approach of Section 2 to limit our sensitivity to any residual biases that remain in the shear catalogue after source selection and implementing the PSF correction of equation (32) (although see below for an additional source selection cut that we have applied based on the strength of the reconstructed PSF anisotropy, prior to construction of our final shear maps).

To limit the impact of very poorly measured and/or noisy shape estimates, we perform an initial source selection on the SDSS galaxy sample. To select galaxies, we follow the works of Bernstein & Jarvis (2002) and Mandelbaum et al. (2008). We thus exclude sources for which the modulus of the corrected ellipticity  $\epsilon = (\epsilon_1^2 + \epsilon_2^2)^{1/2} > 4$  or if the uncertainty in the corrected modulus,  $\sigma_\epsilon > 0.4$ . We also only retain sources that have an i-band extinction that is less than 0.2. In addition, we retain only sources that have both a PSF and DeVaucouleur r-band magnitude greater than 22, and both a PSF and DeVaucouleur i-band magnitude greater than 21.6. Finally, to exclude very small galaxies, we only include sources with  $R_f > 1/3$  where the resolution factor,  $R_f$  is given by,

$$R_f = 1 - \frac{Q_{xx}^{psf} + Q_{yy}^{psf}}{Q_{xx} + Q_{yy}}. \quad (33)$$

With these selection criteria applied,  $\sim 25$  million SDSS sources remain in the catalogue.

#### 4.2.2 Shear systematics and additional source selection

Using the shape information of the remaining SDSS sources we construct maps of the shear components  $\gamma_1$  and  $\gamma_2$  on a  $N_{\text{side}} = 64$  HEALPIX grid using simple averaging, the same as was used in the previous section for the FIRST maps. The resulting maps are shown in Fig. 5. Note that, because of the large increase in galaxy numbers, the noise is much lower in the SDSS maps than in the FIRST maps of Fig. 3. Visual examination of Fig. 5 shows that these initial SDSS shear maps are clearly contaminated with large-scale spurious arcs. Comparing the structure and morphology of these large-scale systematics with a map of the reconstructed PSF anisotropy

reveals a strong correlation, indicating that the observed systematics are residual biases that the approximate correction scheme of equation (32) has failed to account for.

In order to limit the impact of this residual bias, we have implemented an additional cut on the galaxy catalogue based on the strength of the PSF anisotropy at each galaxy position. We discard all remaining SDSS sources for which the reconstructed PSF ellipticity modulus is  $\epsilon > 0.08$ . (We have experimented with this threshold value and have found 0.08 to be the minimum value which still suppresses the systematics to approximately the level of the random noise.) Implementing this additional cut, we were left with  $\sim 9$  million SDSS sources. The SDSS shear maps constructed from this revised catalogue are shown in Fig. 6. Visual inspection of the new maps demonstrate a large reduction in the amplitude of large-scale systematics, which now appear to be at or below the level of the random noise.

This additional cut on the galaxy catalogue increased the noise in the SDSS shear maps by a factor  $\sim \sqrt{3}$ . However, the measured SDSS auto shear power spectrum and the uncertainties associated with the large-scale systematics were reduced by a factor of  $\sim 10$ . Although the FIRST-SDSS cross-power spectrum analysis will be robust to this SDSS-specific systematic effect, suppressing the PSF systematic to the level of the noise at this stage in the analysis is still beneficial in terms of the error performance of the cross-power spectrum analysis: without this additional selection based on the PSF anisotropy amplitude, the uncertainties in the cross-power spectrum increase by a factor of  $\sim 5$  (see Section 6 for more details).

Finally, we generate a weight map for the SDSS survey using the same method as was used in the previous section for the FIRST data. The resulting weight map is shown in Fig. 7 and shows a non-uniform distribution of SDSS source number density. In particular, the very deep coverage of Stripe 82 is clearly visible as an excess of galaxies near the Galactic anti-centre, at declinations  $\delta \sim 0^\circ$ .

## 5 SIMULATIONS

In this section, we describe our approach to creating simulations of the SDSS and FIRST shear datasets. Our simulations serve several purposes. Firstly, the pseudo- $C_\ell$  power spectrum estimator (equation 26) includes a noise-subtraction step which debiases a measurement of the shear power spectrum for the effects of random shape noise (due to both intrinsic galaxy shape noise and measurement errors). For this purpose, we estimate the noise bias,  $\langle \tilde{N}_\ell \rangle_{MC}$

<sup>16</sup> <http://www.sdss3.org/dr10/algorithms/classify.php>



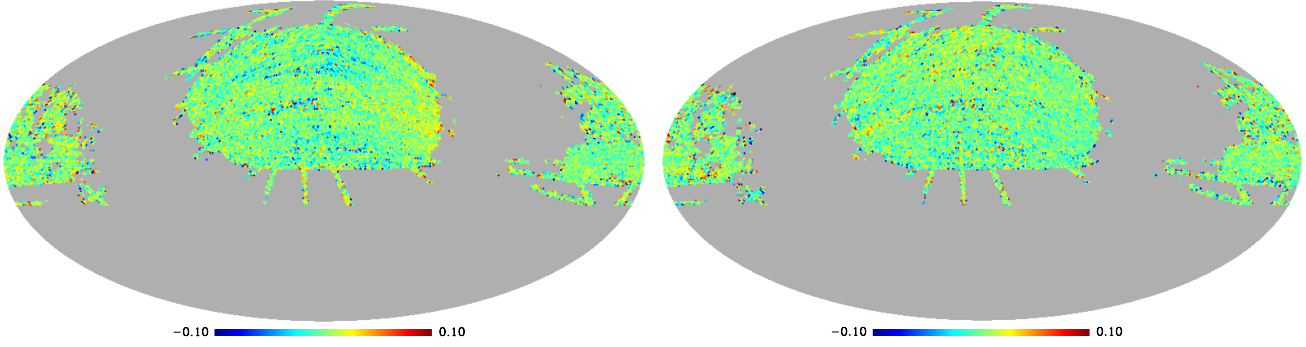


**Figure 6.** Maps of the  $\gamma_1$  (left panel) and  $\gamma_2$  (right panel) shear components, constructed by simple averaging of the SDSS galaxy ellipticities within each pixel. These maps were constructed from the  $\sim 9$  million galaxies remaining in the SDSS shear catalogue immediately after the additional source selection based on the strength of the PSF, described in Section 4.2.2, was implemented. The large-scale systematic effects apparent in Fig. 5 have been substantially reduced with this additional cut on the galaxy catalogue.

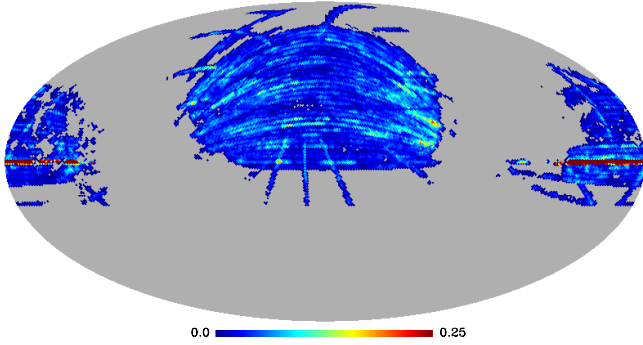


**Figure 7.** The galaxy number density map used to weight the SDSS shear field (Fig. 6) in the power spectrum analysis.

as the average pseudo- $C_\ell$  power spectra measured from a suite of simulations containing realisations of the random shape noise in each survey.

In addition, we will use simulations to estimate the uncertainties on our power spectrum measurements. Given a set of simulations containing both signal and noise components, we estimate the covariance matrix of the power spectrum estimates as:

$$\langle \Delta \hat{P}_b \Delta \hat{P}_{b'} \rangle = \langle (\hat{P}_b - \bar{P}_b)(\hat{P}_{b'} - \bar{P}_{b'}) \rangle_{\text{MC}}, \quad (34)$$

where  $\bar{P}_b$  denotes the average of each band power over all simulations.

Finally, we can also use simulations to validate our power spectrum analysis pipeline and to aid in the interpretation of null tests of the results.

### 5.1 Signal simulations

We generate the signal component of our simulations based on a  $\Lambda$ CDM cosmological model with parameter values taken from Planck Collaboration et al. (2014):  $\Omega_m = 0.3175$ ,  $\sigma_8 = 0.8347$ ,  $H_0 = 67.1 \text{ km s}^{-1} \text{ Mpc}^{-1}$ ,  $\Omega_b = 0.0486$  and  $n_s = 0.963$ , where  $\Omega_m$  and  $\Omega_b$  are the matter and baryon densities,  $\sigma_8$  is the clustering amplitude in  $8 h^{-1} \text{ Mpc}$  spheres,  $H_0$  is the Hubble constant and  $n_s$  is the spectral index of the primordial perturbations. We additionally assume a flat Universe,  $\Omega_\Lambda = 1 - \Omega_m$ .

To generate the input model spectra, we also need to model the redshift distributions of the two surveys. As mentioned earlier,

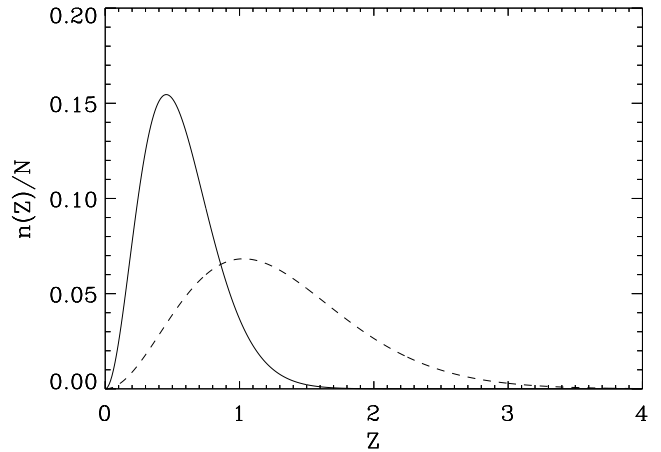


**Figure 8.** Normalised galaxy redshift distributions adopted for the SDSS population (solid line) and for the FIRST population (dashed line). We use these distributions to generate the model shear power spectra for our simulations.

using the  $S^3$  simulation (Wilman et al. 2008) we have estimated the median redshift of the FIRST survey to be  $z_m^{\text{FIRST}} = 1.2$ . For SDSS, we adopt a median redshift for the PHOTO catalogue of  $z_m^{\text{SDSS}} = 0.53$  from Sypniewski (2014). This latter study utilised a method for estimating photometric redshifts using boosted decision trees and the known redshifts of the SDSS SPECTRO sample. We then model both the SDSS and FIRST redshift distributions using the parameterized form,

$$n(z) = \beta \left( \frac{z^2}{z_*^2} \right) \exp \left[ - \left( \frac{z}{z_*} \right)^\beta \right], \quad (35)$$

where  $\beta = 1.5$ ,  $z_* = z_m/1.412$  and  $z_m$  is the assumed median redshift (0.53 for SDSS and 1.2 for FIRST). The resulting redshift distributions are shown in Fig. 8.

Using the above parameter values and  $n(z)$  specifications, we generate the three model shear power spectra (the auto power spectra for the two surveys and the cross-power) according to equation (21). For the 3-D matter power spectrum, we use the Bond & Efstathiou (1984) CDM transfer function. We also use the Halofit formula (Smith et al. 2003) to predict the non-linear  $P_\delta(k, r)$ , although for the scales of interest here, the non-linear contribution is negligible.

We use these power spectra to generate correlated Gaussian realisations of the shear fields in the two surveys. To create the correlated fields, at each multipole,  $\ell$ , we construct the  $2 \times 2$  power spectrum matrix,  $C_\ell^{\kappa(i)\kappa(j)}$  where  $\{i, j\}$  denote the two surveys. Taking the Cholesky decomposition of this matrix at each multipole,  $L_\ell^{ij}$ , defined by

$$C_\ell^{\kappa(i)\kappa(j)} = \sum_k L_\ell^{ik} L_\ell^{jk}, \quad (36)$$

we generate random Gaussian realisations of the spin-2 spherical harmonic coefficients of the two shear fields as

$$\begin{aligned} a_{\ell 0}^i &= \sum_j L_\ell^{ij} G_{\ell 0}^j, \\ a_{\ell m}^i &= \sqrt{\frac{1}{2}} \sum_j L_\ell^{ij} G_{\ell m}^j, \end{aligned} \quad (37)$$

where  $G_{\ell m}^i$  is an array of unit norm complex Gaussian random deviates. The resulting fields transformed to real space via a spin-2 transform will then be correctly correlated according to the input auto and cross-power spectra. When generating the real-space shear fields, we use the same spatial resolution as was used in constructing the shear maps from the real data (HEALPIX  $N_{\text{side}} = 64$ , corresponding to  $0.85 \text{ deg}^2$  pixels).

For each survey, we then create mock galaxy shape catalogues as follows. For each object in the real catalogues, we replace its measured ellipticity components with the components of the simulated shear signal at the appropriate sky location in the HEALPIX-generated maps. Note that we do not randomize the galaxy positions. We choose to keep these fixed as we wish to mimic the real data as closely as possible in the simulations. One aspect of this is that we require the structure in the simulated galaxy number density maps to be the same as that for the real data (see Figs. 4 and 7). The observed large-scale structure in the number density maps is clearly dominated by observational selection effects rather than being due to intrinsic galaxy clustering. It is therefore appropriate to use the exact same number density fluctuations in the simulations in order to capture the impact of these selection effects. Using the unaltered galaxy positions from the real catalogues in all of the simulations ensures that this is the case.

## 5.2 Noise simulations

To create realisations of the random noise, we assign to each simulated galaxy the measured ellipticity components of a real galaxy, sampled at random from the real galaxy catalogues. This procedure should model the random noise properties of the data (due to both the intrinsic dispersion in galaxy shapes and measurement errors in the shape estimation step) and facilitate the estimation of the noise bias term,  $\langle \tilde{N}_\ell \rangle_{\text{MC}}$ . In principle, our procedure may slightly over-estimate the noise since the dispersion in the observed galaxy shapes will be enhanced slightly due to any lensing signal present. However, we expect this effect to have a negligible effect on our analysis – the ellipticity variance due to the combination of intrinsic shape dispersion and measurement errors will greatly dominate over the lensing contribution for any plausible cosmological signal. In any case, our cross-power spectrum measurements are not affected by the noise bias term,  $\langle \tilde{N}_\ell \rangle_{\text{MC}}$ .

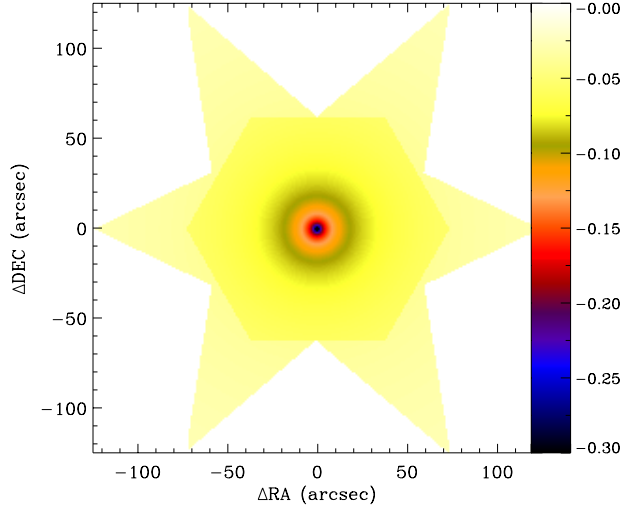


**Figure 9.** The  $\gamma_t$  component of the contamination template used to model the FIRST residual beam systematic discussed in Section 4.1.2, and displayed in Fig. 2. The  $\gamma_r$  component of the contamination was assumed to be zero.

## 5.3 Modelling small-scale systematic effects

In our FIRST simulations, we also include a model of the spurious shear systematic, induced by the FIRST beam residuals, described in Section 4.1.2, and illustrated in Figs. 1 & 2. To model this effect, we first created a template of the observed spurious shear signal. This template is shown in Fig. 9 and has been normalised such that its azimuthally averaged tangential shear profile matches that measured from the real FIRST survey, shown in Fig. 1.

We then use this template to model the contaminating influence of each source detected in the FIRST survey on all other FIRST sources. The spurious signal induced on one source A, due to another source B, is modelled as

$$\begin{aligned} \epsilon_1^{\text{spur}} &= \gamma_t(\Delta RA, \Delta \delta) \cos(2\theta), \\ \epsilon_2^{\text{spur}} &= \gamma_t(\Delta RA, \Delta \delta) \sin(2\theta), \end{aligned} \quad (38)$$

where  $\gamma_t^B(\Delta RA, \Delta \delta)$  is the tangential shear extracted from the template at the position (in  $\{\Delta RA, \Delta \delta\}$ -space) of source A relative to source B. In equation (38),  $\theta$  describes the orientation of the great circle connecting the two sources with respect to the chosen reference axis of the  $\gamma_{1/2}$  coordinate system.

## 5.4 Power spectra from simulations

We create 100 signal-only simulated datasets as described in Section 5.1, each containing a known cosmic shear signal, appropriately correlated between the FIRST and SDSS realisations. Each realisation set also contains a noise-only simulation (Section 5.2) which is uncorrelated between datasets, and a model of the residual FIRST beam systematic which is the same for each realisation (Section 5.3). For each realisation, the sum of all three of these components produces a full mock realisation of the FIRST and SDSS shear catalogues.

We process each simulated catalogue in exactly the same way as we do for the real data. First, maps of the shear components are created from the simulated FIRST and SDSS ellipticities using simple averaging within  $N_{\text{side}} = 64$  HEALPIX pixels. These maps are then multiplied by the appropriate weight maps (Figs. 4 &

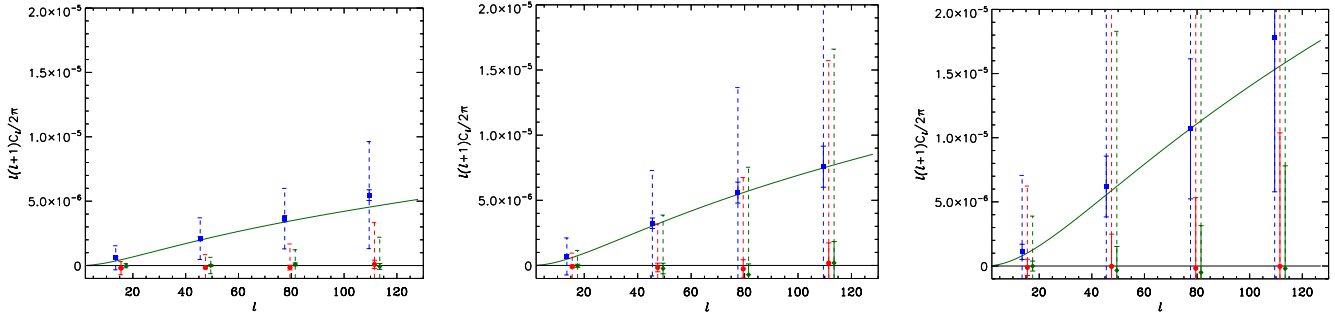


**Figure 10.** The recovered mean SDSS-SDSS (*left*), SDSS-FIRST (*centre*) and FIRST-FIRST (*right*)  $C_\ell^{KK}$  (blue squares),  $C_\ell^{BB}$  (red circles) and  $C_\ell^{KB}$  (green diamonds) power spectra. The solid green curve shows the input  $C_\ell^{KK}$  power spectra. The input  $C_\ell^{BB}$  and  $C_\ell^{KB}$  power spectra were set to zero. Continuous and dashed line error bars show the error in the mean recovered values, and the uncertainty associated with a single realisation or measurement, respectively.

7) before they are passed through the power spectrum estimation pipeline described in Section 2.2.

Fig. 10 shows the mean recovered power spectra from the 100 simulations. We estimate the three possible shear power spectra: the SDSS auto power, the FIRST auto-power and the cross-power between the two surveys. For each of these, in addition to the  $C_\ell^{KK}$  (or *E*-mode) power spectra, we have also measured the  $C_\ell^{BB}$  (or *B*-mode) power and the cross-correlation,  $C_\ell^{KB}$  (or *EB*). We measure the power spectra in four band powers ( $1 < \ell < 32$ ;  $33 < \ell < 64$ ;  $65 < \ell < 96$ ;  $97 < \ell < 128$ ). For each band power we display two error bars: the larger (dashed) errors show the uncertainty associated with a single realisation or measurement (calculated as  $\sigma_{\hat{P}_b} = \langle \hat{P}_b^2 \rangle^{1/2}$  where  $\langle \hat{P}_b^2 \rangle$  are the diagonal elements of the covariance matrix, equation 34) while the smaller errors show the error in the mean recovered band powers,  $\sigma_{\bar{P}_b} = \sigma_{\hat{P}_b} / \sqrt{N_{MC}}$ .

Inspecting the results, we see an unbiased recovery of the input  $C_\ell^{KK}$  signal in all cases while the recovered  $C_\ell^{BB}$  and  $C_\ell^{KB}$  are consistent with zero, as required. The dashed error bars suggests that SDSS has the raw precision to detect the cosmic shear signal on these scales, the cross-power could potentially make a marginal detection while the FIRST dataset is too noisy on its own to detect the signal. Note that, on the relatively large scales of interest here, there is no noticeable effect from the residual beam systematic that we have included in our FIRST simulations. However, we have confirmed with higher resolution simulations that this systematic does bias the recovery of the FIRST auto-power spectrum, and increases the uncertainties on the FIRST-SDSS cross-power spectrum, on smaller angular scales (at higher  $\ell$ ).

### 5.5 Recovery in the presence of large-scale systematics

The results of the previous section demonstrate that our power spectrum analysis can recover a known input signal in the presence of both random noise and the small-scale FIRST systematic. Those results also show that our analysis correctly accounts for the effects of the finite sky coverage and masking of the data.

However, visual inspection of Figs. 3 & 6 suggests that there are additional large-scale systematics present in the data that are not modelled by our simulations. Our approach to dealing with these systematics is a central theme of this paper: by measuring the FIRST-SDSS cross-power spectrum, these systematics should drop out of the analysis, provided that the FIRST and SDSS systematic effects are uncorrelated. To quantify the advantages of this

approach, here we demonstrate the unbiased recovery of a simulated cross-power spectrum signal in the presence of either the real SDSS or the real FIRST large-scale systematic effects.

To demonstrate unbiased recovery of the cross-power spectrum in the presence of the SDSS systematics, we superimpose the SDSS signal-only simulations onto the real SDSS map. Along with any signals present in the real data (cosmic shear, noise and systematics), the resulting coadded maps will now also contain a simulated signal that is correlated with that present in the FIRST simulations. We have passed these coadded “real + simulated” maps through our power spectrum estimation pipeline and the results are shown in Fig. 11. These recovered power spectra have undergone noise-bias subtraction and correction of the mask in exactly the same way as before. Fig. 11 shows that the recovery of the SDSS auto power spectrum is very heavily biased by the presence of unaccounted-for large-scale systematics in the data.<sup>17</sup> However, the right hand panel of Fig. 11 shows that the recovery of the SDSS-FIRST cross-power spectrum remains unbiased, despite the presence of the SDSS systematics. Note that, although it is unbiased, the cross-power spectrum is not completely unaffected by the presence of the SDSS systematics: their presence results in a significant increase in the error bars of the cross-power spectrum recovery (compare the right-hand panel of Fig. 11 and the central panel of Fig. 10), due to chance correlations between the noise in the FIRST simulations and the SDSS systematic effects. We will account for these additional contributions to the errors in our final analysis.

To assess the impact of the large-scale systematics in the FIRST shear maps, we have performed an equivalent analysis to what is described above but now we superimpose the FIRST signal-only simulations onto the real FIRST maps and cross-correlate these with the SDSS simulations. The results of this test are displayed in Fig. 12 where we observe similar effects to what is described above – the FIRST auto-power spectrum is heavily biased by large-scale systematics while the cross-power spectrum remains unbiased.

<sup>17</sup> The alternative explanation – that the power observed in the left hand panel of Fig. 11 is of cosmological origin – is ruled out given current CMB and large-scale structure observations, and in any case is incompatible with the FIRST-SDSS cross-power spectrum that we measure later. The very large  $C_\ell^{BB}$  signal observed is a further strong indicator that the observed  $C_\ell^{KK}$  signal in the SDSS auto power spectrum is due to large-scale systematics.

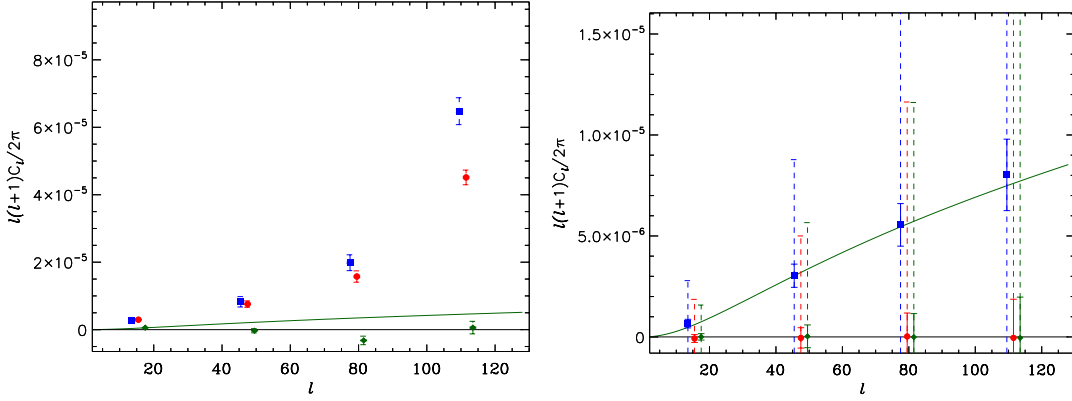


**Figure 11.** The recovered mean SDSS auto power spectra (*left panel*) and SDSS-FIRST cross-power spectra (*right panel*) from 100 simulations in the presence of large-scale systematic effects in the real SDSS shear maps. For a definition of the symbols see Fig. 10. Systematic effects in the SDSS data severely bias the recovery of the auto power spectrum, shown as the solid curve in the left hand panel. The cross-power spectrum recovery is unbiased in the presence of the same systematics, though the errors are amplified.

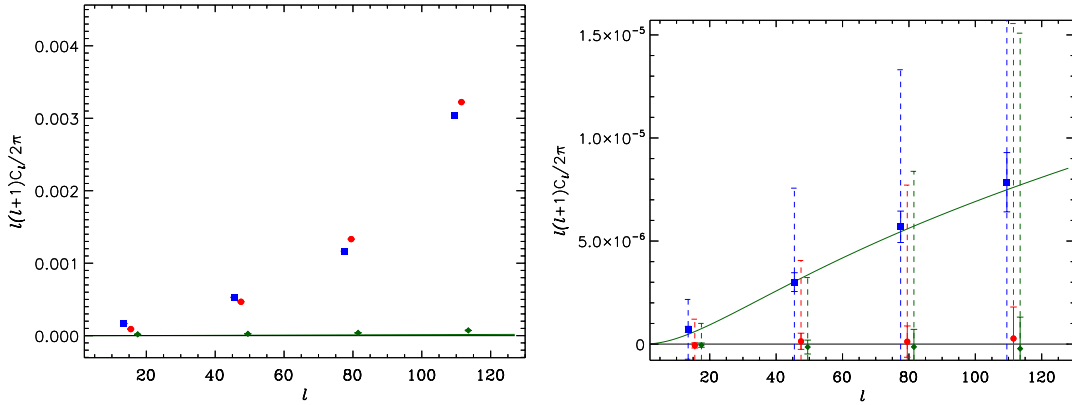


**Figure 12.** The recovered mean FIRST auto power spectra (*left panel*) and SDSS-FIRST cross-power spectra (*right panel*) from 100 simulations in the presence of large-scale systematic effects in the real FIRST shear maps. For a definition of the symbols see Fig. 10. Systematic effects in the FIRST data severely bias the recovery of the auto power spectrum, shown as the solid curve in the left hand panel. As in Fig. 11, the systematics contribute additional errors into the cross-power spectrum measurement though it remains unbiased.

## 6 REAL DATA MEASUREMENTS

In the previous section, we have demonstrated, using simulations, that we can extract an unbiased cosmic shear signal by cross-correlating the two datasets even in the presence of significant systematic effects in both surveys, provided that the SDSS and FIRST systematics are not correlated with one another. We now apply the analysis to the real datasets.

### 6.1 The SDSS-FIRST cross-power spectra

To extract the cross-power spectrum from the real data, we apply the exact same procedure as was followed for measuring the power spectrum from the simulations in the previous section. Explicitly, we apply the power spectrum estimator of equation (26) to the real data maps, including both the noise debiasing step (based on the mean noise bias,  $\langle N_{MC} \rangle$ , measured from noise only simulations) and the correction for the survey geometries and masks.

To estimate errors, we once again use the scatter in the MC simulations (equation 34). However, in addition to the normal cosmic variance and noise terms, we now also wish to include the enhanced uncertainties due to chance correlations between random

noise and large-scale systematics discussed in Section 5.5. To facilitate this, we generate the *total* mock cross-power spectrum for the each simulation realisation as

$$\hat{P}_b^i = \hat{P}_b(\text{sim}_F^i \times \text{sim}_S^i) + \hat{P}_b(\text{sim}_F^i \times \text{real}_S) + \hat{P}_b(\text{real}_F \times \text{sim}_S^i), \quad (39)$$

where  $\hat{P}_b(\text{sim}_F^i \times \text{sim}_S^i)$  is the cross-power spectrum measured from the  $i^{\text{th}}$  simulation set containing both signal and noise,  $\hat{P}_b(\text{sim}_F^i \times \text{real}_S)$  is the power spectrum measured by cross-correlating the  $i^{\text{th}}$  FIRST simulation with the real SDSS map, and  $\hat{P}_b(\text{real}_F \times \text{sim}_S^i)$  is the power spectrum measured by cross-correlating the  $i^{\text{th}}$  SDSS simulation with the real FIRST map. The covariance matrix of our measurements can then be calculated from the scatter amongst the total mock power spectra of equation (39), and will now include uncertainties due to cosmic variance, random noise and the enhanced uncertainties due to the systematic effects.

The cross-spectrum measured from the real FIRST and SDSS datasets is shown in Fig. 13. Comparing the real data measurement to the distribution of measured power spectra from simulations that include only noise and systematics, we find our measurement equates to a marginal detection of the  $C_\ell^{KK}$  power spectrum at the 99% confidence level (a “ $\sim 2.7\sigma$  detection”). The measured signal is in agreement (within  $\sim 1\sigma$ ) with the model theory power



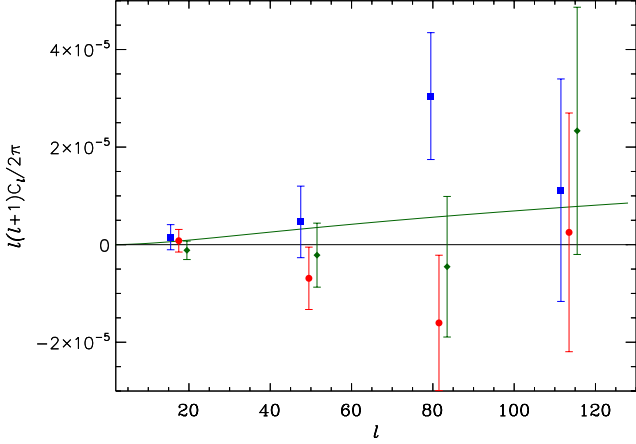


**Figure 13.** The cosmic shear cross-power spectrum measured from the SDSS and FIRST datasets. The blue squares show the measured  $E$ -mode signal ( $C_\ell^{kk}$ ), the red circles show the measured  $B$ -mode ( $C_\ell^{\beta\beta}$ ) and the green diamonds show the measured  $EB$  correlation  $C_\ell^{k\beta}$ . The green solid curve is the expected  $C_\ell^{kk}$  power spectrum for two populations with median redshifts of 0.53 and 1.2 respectively.

spectrum where the median redshifts for the SDSS and FIRST populations are assumed to be 0.53 and 1.2 respectively. The  $B$ -mode power spectrum ( $C_\ell^{\beta\beta}$ ) and the  $EB$  cross-correlation ( $C_\ell^{k\beta}$ ) are both consistent with zero (within  $\sim 1\sigma$ ).

To further assess the significance of our measurement and the degree to which it is consistent with the expected signal in the concordance cosmological model, we have calculated a  $\chi^2$  statistic from our suite of total simulated power spectra (equation 39) as:

$$\chi^2 = \sum_b (\hat{P}_b - P_b^{\text{th}})^2 / \sigma_{\hat{P}_b}^2, \quad (40)$$

where  $P_b^{\text{th}}$  is the expected value of the band power in the concordance model. We then compare the  $\chi^2$  value measured from the real data to the distribution of values from the simulated data sets. We have calculated this statistic for the three power spectra ( $C_\ell^{kk}$ ,  $C_\ell^{\beta\beta}$  and  $C_\ell^{k\beta}$ ) separately and note that, for the latter two spectra,  $P_b^{\text{th}} = 0$ . The results of this test are shown in the top panels of Fig. 14. We see that our measurement from the real data is consistent with the simulation distribution, and hence with the expectation based on the concordance cosmology.

The  $\chi^2$  statistic tests for a particular type of discrepancy between model and data. However, it does not test for all possible deviations. In particular, it is insensitive to the sign of  $\hat{P}_b - P_b^{\text{th}}$ . We have therefore also performed a consistency test using the following statistic (which we loosely call  $\chi$ ):

$$\chi = \sum_b (\hat{P}_b - P_b^{\text{th}}) / \sigma_{\hat{P}_b}. \quad (41)$$

The results from this test are shown in the lower panels of Fig. 14 and once again, reveal no inconsistencies between our measurements and the concordance cosmological model.

## 6.2 Null tests

We further assess the credibility of the data and results through a set of measurements designed to reveal any residual systematics that, for whatever reason, might not be mitigated using our cross-power spectrum approach. For each of these null tests, we have processed

each of our simulated datasets in exactly the same way in order to assign appropriate error bars to the null test measurements. The tests that we have performed are the following:

(i) *North-South*: We split both the SDSS and FIRST data into North and South samples, with roughly the same number of sources in each sample. We then measure the power spectra for the two samples separately. Finally we subtract the signal between the two sets of spectra.

(ii) *East-West*: This is the same as test (i) but splitting the data into East and West components.

(iii) *FIRST random*: We randomly split the FIRST data into two subsets with the same number of galaxies. For each subset, a set of  $\gamma_1$  and  $\gamma_2$  maps is then created. We take the difference of the shear maps for the two FIRST subsets and then estimate the cross-power spectrum of the resulting residual map with the SDSS shear map.

(iv) *SDSS random*: The same as test (iii) but randomly splitting the SDSS data.

(v) *FIRST PSF*: This test is designed to test whether the measured signal is an artefact of the FIRST PSF. In addition to deconvolved shape estimates, the FIRST catalogue also includes estimates of source shapes before PSF deconvolution. We replace our FIRST galaxy ellipticity catalogue with an ellipticity catalogue based on these uncorrected shape measurements for only those sources that are flagged as point sources (unresolved) in FIRST. The shear maps constructed from this catalogue should then trace the FIRST PSF accurately. We then estimate the cross-power spectrum of the FIRST PSF map and SDSS shear catalogue.

(vi) *SDSS PSF*: To test for artefacts associated with the SDSS PSF, we construct SDSS PSF maps using the quoted values in the SDSS survey for the reconstructed PSF at the location of each galaxy. The resulting PSF ellipticity maps are then cross-correlated with the FIRST shear catalogue.

(vii) *FIRST  $P(S) > 0.05$* : This final test is not strictly a null test. However, we implement it to test for any dependence of our measurement on the likelihood of the FIRST sources being sidelobe residuals. To perform this test, we create an alternate FIRST shape catalogue based on only those sources that have a higher chance of being a sidelobe,  $P(S) > 0.05$ . (Recall our main analysis is based on only sources with  $P(S) < 0.05$ .) We then repeat the FIRST-SDSS cross-power spectrum analysis using the  $P(S) > 0.5$  alternative FIRST catalogue.

The  $C_\ell^{kk}$ ,  $C_\ell^{\beta\beta}$  and  $C_\ell^{k\beta}$  power spectra measured for all of these tests are shown in Fig. 15. In order to interpret these null tests, in Fig. A1, we once again plot the  $\chi^2$  measurement from the real data alongside the  $\chi^2$  histograms from the simulations. When calculating the  $\chi^2$  values for the null tests, we set  $P_b^{\text{th}} = 0$  in equation (40). Examination of Figs. 15 and A1 show that the data passes most of these null tests in the sense that the  $\chi^2$  values from the real data are usually consistent with being a random sample of the simulation  $\chi^2$  distribution. Potential problem cases are the *East-West*  $C_\ell^{\beta\beta}$  and *SDSS PSF*  $C_\ell^{k\beta}$  null tests. However, taken as a population, these tests do not reveal any major outstanding problems in the cross-power spectrum results. To further quantify the results of these tests, in Table 1, we list the probability to exceed (PTE) values for each test, which gives the probability that the  $\chi^2$  value measured from the real data is consistent with being a random sampling of the simulation distribution. Low values of these PTE numbers indicate potential residual systematics. For completeness, in Fig. A2, we also present the measurements of  $\chi$  (equation 41 with  $P_b^{\text{th}} = 0$ ) from the real data along with the simulation histograms. These tests reveal no obvious problems with the analysis.

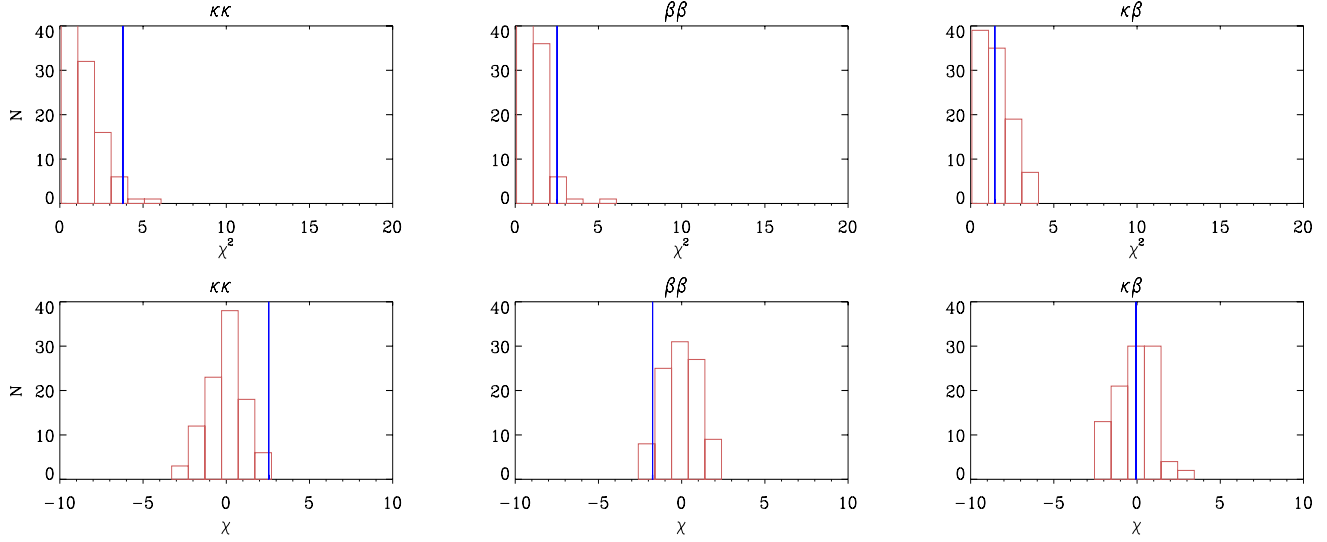


**Figure 14.** Histograms showing the  $\chi^2$  values (equation 40; upper panels) and  $\chi$  values (equation 41; lower panels) for the  $C_\ell^{KK}$  (left),  $C_\ell^{BB}$  (centre) and  $C_\ell^{KB}$  (right) power spectra as measured from the simulations. Over-plotted as the vertical blue line is the equivalent value for the real data measurements.

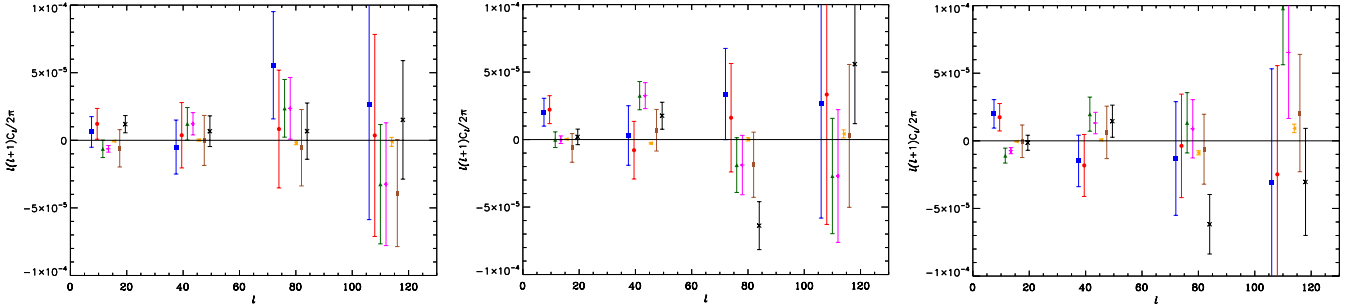


**Figure 15.** The  $C_\ell^{KK}$  (left),  $C_\ell^{BB}$  (centre) and  $C_\ell^{KB}$  (right) power spectra measurements for the null tests described in Section 6.2. The displayed results are as follows: *North-South*: blue squares; *East-West*: red circles; *FIRST random*: green face up triangles; *SDSS random*: magenta horizontal lines; *FIRST PSF*: orange face left triangles; *SDSS PSF*: brown rectangles; *FIRST  $P(S)>0.05$* : black crosses.

**Table 1.** PTE values from the  $\chi^2$  null tests described in Section 6.2.

Null test	$C_\ell^{KK}$	$C_\ell^{BB}$	$C_\ell^{KB}$
<i>North-South</i> :	0.64	0.10	0.10
<i>East-West</i> :	0.81	0.01	0.12
<i>FIRST random</i> :	0.41	0.53	0.52
<i>SDSS random</i> :	0.35	0.10	0.19
<i>FIRST PSF</i> :	0.96	0.85	0.87
<i>SDSS PSF</i> :	0.18	0.67	0.02
<i>FIRST <math>P(S)&gt;0.05</math></i> :	0.35	0.31	0.99

### 6.3 Constraints on the FIRST and SDSS median redshifts, $\sigma_8$ and $\Omega_m$

Having demonstrated the validity of our results using null tests, we now use our cross-power spectrum measurement to constrain the median redshifts of the two populations, and the power spectrum normalisation,  $\sigma_8$  and matter density,  $\Omega_m$ .

To constrain the median redshifts of FIRST and SDSS we perform a grid-based likelihood analysis and generate the  $C_\ell^{KK}$  spec-

trum for two populations with median redshifts in the range  $0.05 < z_m^{\text{SDSS}} < 5.05$  and  $0.5 < z_m^{\text{FIRST}} < 5.5$ . The grid resolution in both directions is  $\Delta_z = 0.01$ . We fix the cosmological parameters values at  $\sigma_8 = 0.8347$  and  $\Omega_m = 0.3175$  (Planck Collaboration et al. 2014). The model FIRST-SDSS cross-power spectrum is generated using equation (21) and is then averaged in band powers similarly to what was done during the power spectrum estimation.

For each point in parameter space, we construct the  $\chi^2$  misfit statistic (equation 40) which we then convert to likelihood values for a model with two degrees of freedom. The results are shown in Fig. 16. We immediately see that the constraints are symmetric about the  $z_m^{\text{SDSS}} = z_m^{\text{FIRST}}$  line. However, for the purposes of this study we will make the reasonable assumption that  $z_m^{\text{SDSS}} < z_m^{\text{FIRST}}$ . With this prior in place, the best fitting values for the median redshifts are  $z_m^{\text{SDSS}} = 1.5$  and  $z_m^{\text{FIRST}} = 1.75$ . However, the data are also entirely consistent (within  $1\sigma$ ) with the median redshifts derived from the literature of  $z_m^{\text{SDSS}} = 0.53$  (Sypniewski 2014) and  $z_m^{\text{FIRST}} = 1.2$  (Wilman et al. 2008).

We now fix the median redshifts for SDSS and FIRST to the literature values ( $z_m^{\text{SDSS}}=0.53$  and  $z_m^{\text{FIRST}}=1.2$ ) and use our  $C_\ell^{KK}$  measurements to place constraints on the cosmological parameters,  $\sigma_8$

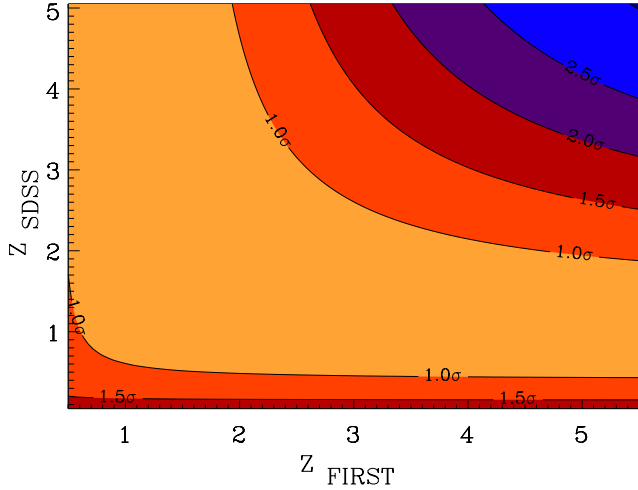


**Figure 16.** Joint constraints on the median redshifts of the SDSS and FIRST surveys obtained from fitting theoretical models to our  $C_\ell^{kk}$  cross-power spectrum measurements. Cosmological parameters were kept fixed at the concordance values reported in Planck Collaboration et al. (2014).

and  $\Omega_m$ . The results are shown in Fig. 17. The best fitting values for the two parameters are  $\sigma_8 = 1.5^{+0.6}_{-0.8}$  (68%) and  $\Omega_m = 0.3^{+0.3}_{-0.2}$  (68%). Our results are in agreement with the values in Planck Collaboration et al. (2014) at the  $1\sigma$  level. Our results are also in good agreement with the  $\sigma_8$  constraint obtained from the FIRST cosmic shear analysis of Chang et al. (2004).

## 7 CONCLUSIONS

We have presented a cosmic shear cross-power spectrum analysis of the SDSS and FIRST surveys, a pair of optical and radio sky surveys with approximately 10,000 deg<sup>2</sup> of overlapping sky coverage.

The motivation for our study has been to demonstrate the power of optical-radio cross-correlation analyses for mitigating systematic effects in cosmic shear analyses. The shear maps that we have constructed from both the SDSS and the FIRST catalogues are severely affected by systematic effects. Measuring the auto-shear power spectrum from either of the datasets results in a heavily biased measurement – in both cases, the measured convergence power spectrum,  $C_\ell^{kk}$  is more than an order of magnitude larger than that expected in the concordance cosmological model. The presence of a large  $B$ -mode signal ( $C_\ell^{\beta\beta}$ ) in both the SDSS and FIRST auto power spectra is further evidence that the shear maps are contaminated by large-scale systematic effects. For our SDSS maps, these large-scale systematics dominate over the random noise on the scales of interest here ( $\ell < 120$ ). For FIRST, the spurious power due to the large-scale systematics is approximately the same as the noise power spectrum. Note however that the random noise component in the FIRST shear maps is much larger than in the SDSS maps due to the much small galaxy number density in FIRST. Despite these very large shear systematics, we have demonstrated using simulations that one can still recover a cosmic shear signal using the FIRST-SDSS cross-power spectrum. Although the cross-power spectrum is not affected by uncorrelated systematics in the mean, the associated uncertainties on the cross-power spectrum measurements are amplified by the presence of the FIRST and SDSS systematic effects. In our final analysis, our total errors on  $C_\ell^{kk}$  have increased by a factor of  $\sim 2.5$  compared to those due to

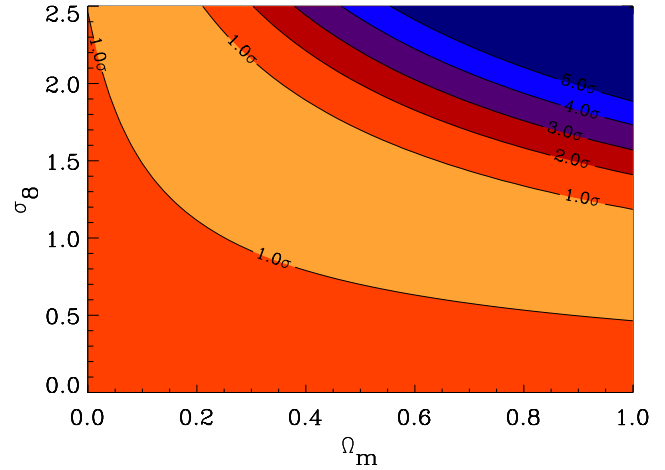


**Figure 17.** Joint constraints on the matter density,  $\Omega_m$  and power spectrum normalisation,  $\sigma_8$  from fitting theoretical models to our  $C_\ell^{kk}$  cross-power spectrum measurements. The median redshifts were fixed at  $z_m^{\text{SDSS}} = 0.53$  and  $z_m^{\text{FIRST}} = 1.2$ .

cosmic variance and random noise alone. Although not the focus of this paper, it is likely that this enhancement in the cross-power spectrum errors could be significantly reduced by applying more sophisticated techniques for correcting the galaxy shapes measurements for the effects of PSF anisotropy in both surveys, prior to construction of the final shear maps.

By cross-correlating the SDSS and the FIRST data, we tentatively detect a signal in the  $C_\ell^{kk}$  power spectrum that is inconsistent with zero at the 99% confidence level. In contrast to almost all cosmic shear analyses to date (which primarily probe the shear signal on sub-degree scales), our measurements constrain the weak lensing power spectrum on large angular scales. Our measurements probe the power spectrum in the fully linear régime, in the multipole range  $10 \lesssim \ell \lesssim 100$ , corresponding to angular scales  $2^\circ \lesssim \theta \lesssim 20^\circ$ .

Our results are consistent (within  $\sim 1\sigma$ ) with the expected signal in the concordance cosmological model, assuming median redshifts of  $z_m^{\text{SDSS}} = 0.53$  and  $z_m^{\text{FIRST}} = 1.2$  for the SDSS and FIRST surveys respectively. Our measurements of the odd-parity ( $C_\ell^{\beta\beta}$ ) and parity-violating ( $C_\ell^{\kappa\beta}$ ) cross-power spectra are fully consistent with zero, which demonstrates the success of the cross-power spectrum approach in mitigating systematic effects. We have also validated our analysis and results by performing a range of null tests on the data.

We have used our  $C_\ell^{kk}$  measurement to jointly constrain the median redshifts of the two surveys. With cosmological parameters fixed at their concordance values and assuming  $z_m^{\text{SDSS}} < z_m^{\text{FIRST}}$ , we find best fitting value of  $z_m^{\text{SDSS}} = 1.5$  and  $z_m^{\text{FIRST}} = 1.75$ . However, our constraints are weak and our measurements are also consistent with the literature values of  $z_m^{\text{SDSS}} = 0.53$  and  $z_m^{\text{FIRST}} = 1.2$ . Fixing the median redshifts to these literature values, we have used our measurements to constrain the cosmological parameters  $\Omega_m$  and  $\sigma_8$ , where we find best fitting values of  $\Omega_m = 0.30^{+0.3}_{-0.2}$  and  $\sigma_8 = 1.5^{+0.6}_{-0.8}$  (68% confidence levels), which are consistent with values quoted in Planck Collaboration et al. (2014) at the  $1\sigma$  level.

Although the detection of  $C_\ell^{kk}$  presented here is tentative and lacks the precision achieved by state-of-the-art optical weak lensing surveys, we believe the analysis techniques developed in this paper will prove extremely useful for future high precision cosmic

shear analyses. In particular, we have successfully demonstrated that one can extract an unbiased cosmic shear signal even in the presence of severe shear systematics using the cross-power spectrum approach. This type of analysis will be well suited for performing cross-correlation studies of future overlapping optical and radio surveys (e.g. with SKA, LSST and *Euclid*). Cosmic shear analyses of these future surveys will require exquisite control of systematic effects if they are to meet their science goals of per cent level constraints on dark energy and modified gravity theories. The cross-power spectrum approach that we have demonstrated for the first time in this paper represents a very promising tool for achieving the required control of systematic effects.

## ACKNOWLEDGMENTS

We thank Neal Jackson, Ian Harrison, Nick Wrigley and Stuart Harper for useful discussions. CD acknowledges the support of a STFC quota studentship and a President's Doctoral Scholarship from the University of Manchester. CD and MLB are grateful to the European Research Council for support through the award of an ERC Starting Independent Researcher Grant (EC FP7 grant number 280127). MLB also thanks the STFC for the award of Advanced and Halliday fellowships (grant number ST/I005129/1).

Funding for SDSS-III has been provided by the Alfred P. Sloan Foundation, the Participating Institutions, the National Science Foundation, and the U.S. Department of Energy Office of Science. The SDSS-III web site is <http://www.sdss3.org/>.

SDSS-III is managed by the Astrophysical Research Consortium for the Participating Institutions of the SDSS-III Collaboration including the University of Arizona, the Brazilian Participation Group, Brookhaven National Laboratory, Carnegie Mellon University, University of Florida, the French Participation Group, the German Participation Group, Harvard University, the Instituto de Astrofísica de Canarias, the Michigan State/Notre Dame/JINA Participation Group, Johns Hopkins University, Lawrence Berkeley National Laboratory, Max Planck Institute for Astrophysics, Max Planck Institute for Extraterrestrial Physics, New Mexico State University, New York University, Ohio State University, Pennsylvania State University, University of Portsmouth, Princeton University, the Spanish Participation Group, University of Tokyo, University of Utah, Vanderbilt University, University of Virginia, University of Washington, and Yale University.

Some of the results in this paper have been derived using the HEALPix (Górski et al. 2005) package.

## REFERENCES

- Abazajian, K., Adelman-McCarthy, J. K., Agüeros, M. A., et al., 2003, *AJ*, 126, 2081, astro-ph/0305492
- Ahn, C. P., Alexandroff, R., Allende Prieto, C., et al., 2014, *ApJS*, 211, 17, arXiv:1307.7735
- Aubourg, É., Bailey, S., Bautista, J. E., et al., 2014, *ArXiv e-prints*, arXiv:1411.1074
- Bacon, D. J., Massey, R. J., Refregier, A. R., Ellis, R. S., 2003, *MNRAS*, 344, 673, astro-ph/0203134
- Bacon, D. J., Refregier, A. R., Ellis, R. S., 2000, *MNRAS*, 318, 625, arXiv:astro-ph/0003008
- Bartelmann, M., Schneider, P., 2001, *Phys. Rep.*, 340, 291, astro-ph/9912508
- Becker, R. H., White, R. L., Helfand, D. J., 1995, *ApJ*, 450, 559
- Bernstein, G. M., Jarvis, M., 2002, *AJ*, 123, 583, astro-ph/0107431
- Blandford, R. D., Saust, A. B., Brainerd, T. G., Villumsen, J. V., 1991, *MNRAS*, 251, 600
- Bond, J. R., Efstathiou, G., 1984, *ApJL*, 285, L45
- Brown, M. L., Abdalla, F. B., Amara, A., et al., 2013, *ArXiv e-prints*, arXiv:1312.5618
- Brown, M. L., Bacon, D. J., Camera, S., et al., 2015, *ArXiv e-prints*, arXiv:1501.03828
- Brown, M. L., Battye, R. A., 2011, *MNRAS*, 410, 2057, arXiv:1005.1926
- Brown, M. L., Castro, P. G., Taylor, A. N., 2005, *MNRAS*, 360, 1262, astro-ph/0410394
- Brown, M. L., Taylor, A. N., Bacon, D. J., et al., 2003, *MNRAS*, 341, 100, astro-ph/0210213
- Chang, T.-C., Refregier, A., Helfand, D. J., 2004, *ApJ*, 617, 794, arXiv:astro-ph/0408548
- Dawson, K. S., Schlegel, D. J., Ahn, C. P., et al., 2013, *AJ*, 145, 10, arXiv:1208.0022
- Eisenstein, D. J., Weinberg, D. H., Agol, E., et al., 2011, *AJ*, 142, 72, arXiv:1101.1529
- Fischer, P., McKay, T. A., Sheldon, E., et al., 2000, *AJ*, 120, 1198, astro-ph/9912119
- Fu, L., Semboloni, E., Hoekstra, H., et al., 2008, *A&A*, 479, 9, arXiv:0712.0884
- Górski, K. M., Hivon, E., Banday, A. J., et al., 2005, *ApJ*, 622, 759, astro-ph/0409513
- Gunn, J. E., 1967, *ApJ*, 150, 737
- Heymans, C., Van Waerbeke, L., Miller, L., et al., 2012, *MNRAS*, 427, 146, arXiv:1210.0032
- Hirata, C., Seljak, U., 2003, *MNRAS*, 343, 459, astro-ph/0301054
- Hoekstra, H., Mellier, Y., van Waerbeke, L., et al., 2006, *ApJ*, 647, 116, astro-ph/0511089
- Högbom, J. A., 1974, *A&AS*, 15, 417
- Huff, E. M., Eifler, T., Hirata, C. M., Mandelbaum, R., Schlegel, D., Seljak, U., 2014, *MNRAS*, 440, 1322
- Jarvis, M., Jain, B., 2008, *JCAP*, 1, 003, arXiv:0706.4316
- Jee, M. J., Tyson, J. A., Schneider, M. D., Wittman, D., Schmidt, S., Hilbert, S., 2013, *ApJ*, 765, 74, arXiv:1210.2732
- Joachimi, B., Cacciato, M., Kitching, T. D., et al., 2015, *ArXiv e-prints*, arXiv:1504.05456
- Kaiser, N., 1998, *ApJ*, 498, 26, arXiv:astro-ph/9610120
- Kaiser, N., Squires, G., 1993, *ApJ*, 404, 441
- Kaiser, N., Wilson, G., Luppino, G. A., 2000, *ArXiv Astrophysics e-prints*, arXiv:astro-ph/0003338
- Kiessling, A., Cacciato, M., Joachimi, B., et al., 2015, *ArXiv e-prints*, arXiv:1504.05546
- Kilbinger, M., Fu, L., Heymans, C., et al., 2013, *MNRAS*, 430, 2200, arXiv:1212.3338
- Kirk, D., Brown, M. L., Hoekstra, H., et al., 2015, *ArXiv e-prints*, arXiv:1504.05465
- Lin, H., Dodelson, S., Seo, H.-J., et al., 2012, *ApJ*, 761, 15, arXiv:1111.6622
- Mandelbaum, R., Seljak, U., Hirata, C. M., 2008, *JCAP*, 8, 006, arXiv:0805.2552
- Mandelbaum, R., Seljak, U., Kauffmann, G., Hirata, C. M., Brinkmann, J., 2006, *MNRAS*, 368, 715, astro-ph/0511164
- Newman, E. T., Penrose, R., 1966, *Journal of Mathematical Physics*, 7, 863
- Patel, P., Bacon, D. J., Beswick, R. J., Muxlow, T. W. B., Hoyle, B., 2010, *MNRAS*, 401, 2572, arXiv:0907.5156



- Planck Collaboration, Ade, P. A. R., Aghanim, N., et al., 2014, *A&A*, 571, A16, arXiv:1303.5076
- Pourtsidou, A., Metcalf, R. B., 2014, *MNRAS*, 439, L36, arXiv:1311.4484
- Rozo, E., Wechsler, R. H., Rykoff, E. S., et al., 2010, *ApJ*, 708, 645, arXiv:0902.3702
- Schneider, P., 1998, *ApJ*, 498, 43, arXiv:astro-ph/9708269
- Schrabback, T., Hartlap, J., Joachimi, B., et al., 2010, *A&A*, 516, A63, arXiv:0911.0053
- Sheldon, E. S., Johnston, D. E., Scranton, R., et al., 2009, *ApJ*, 703, 2217, arXiv:0709.1153
- Skrutskie, M. F., Cutri, R. M., Stiening, R., et al., 2006, *AJ*, 131, 1163
- Smith, R. E., Peacock, J. A., Jenkins, A., et al., 2003, *MNRAS*, 341, 1311, astro-ph/0207664
- Sypniewski, A. J., 2014, Optimizing Photometric Redshift Estimation for Large Astronomical Surveys Using Boosted Decision Trees
- Van Waerbeke, L., Mellier, Y., Erben, T., et al., 2000, *A&A*, 358, 30, arXiv:astro-ph/0002500
- Van Waerbeke, L., Mellier, Y., Radovich, M., et al., 2001, *A&A*, 374, 757, astro-ph/0101511
- Villumsen, J. V., 1995, *ArXiv Astrophysics e-prints*, astro-ph/9507007
- Wilman, R. J., Miller, L., Jarvis, M. J., et al., 2008, *MNRAS*, 388, 1335, arXiv:0805.3413
- Wittman, D. M., Tyson, J. A., Kirkman, D., Dell’Antonio, I., Bernstein, G., 2000, *Nature*, 405, 143, arXiv:astro-ph/0003014
- York, D. G., Adelman, J., Anderson, J. E., Jr., et al., 2000, *AJ*, 120, 1579, astro-ph/0006396

## APPENDIX A: RESULTS FROM NULL TESTS

Fig. A1 compares the  $\chi^2$  statistic (equation 40)) for the data with the distribution of  $\chi^2$  measured from the simulations for the suite the null tests described in Section 6.2. Fig. A2 shows the same comparison for the  $\chi$  statistic of equation (41).

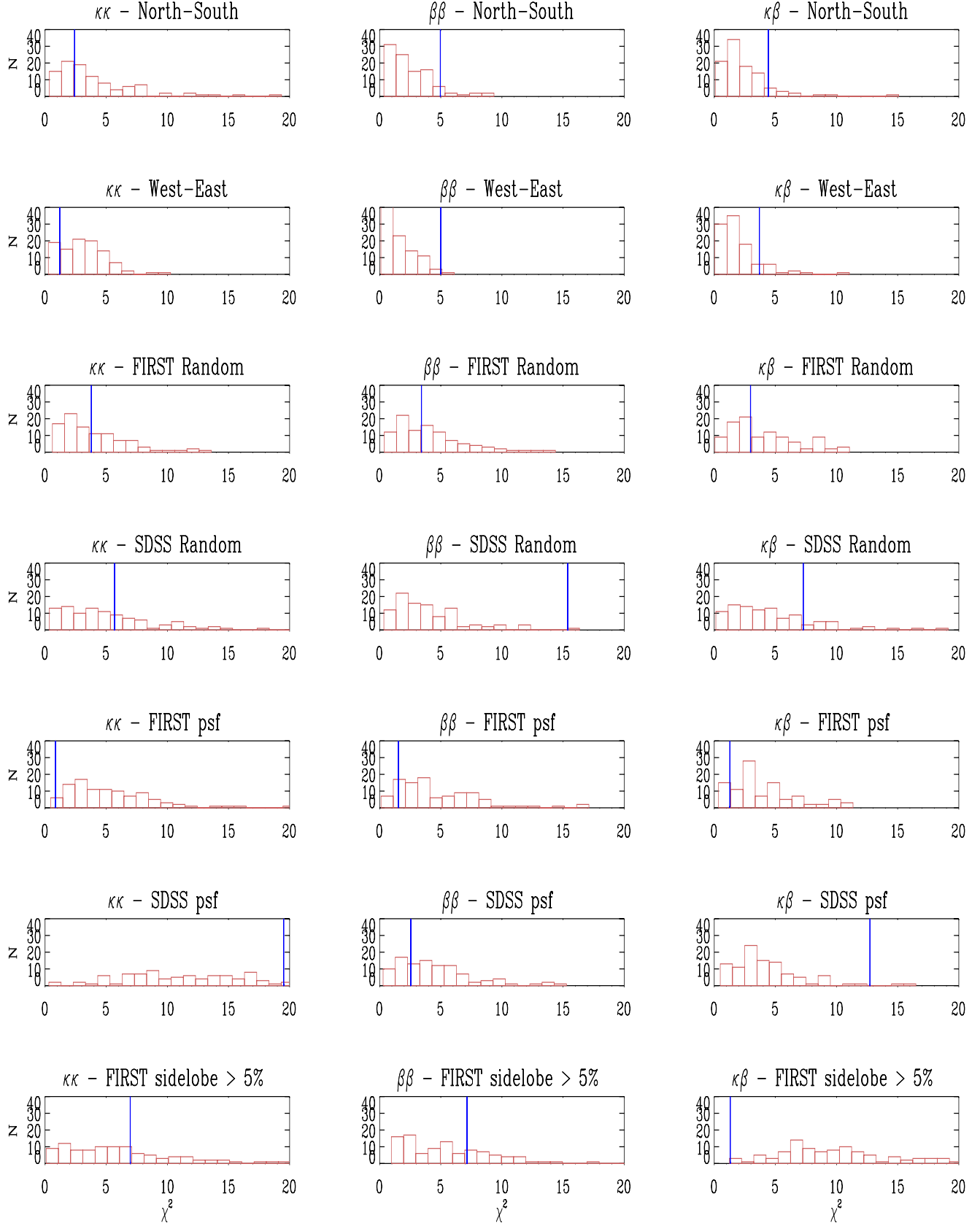


**Figure A1.** Histograms showing the distribution of  $\chi^2$  values (equation 40) measured from the simulations for the suite of null tests described in Section 6.2. The results are shown for the  $C_{\ell}^{\kappa\kappa}$  (left column),  $C_{\ell}^{\beta\beta}$  (centre column) and  $C_{\ell}^{\kappa\beta}$  (right column) power spectra. Over-plotted as the vertical blue line is the equivalent value for the real data measurement.

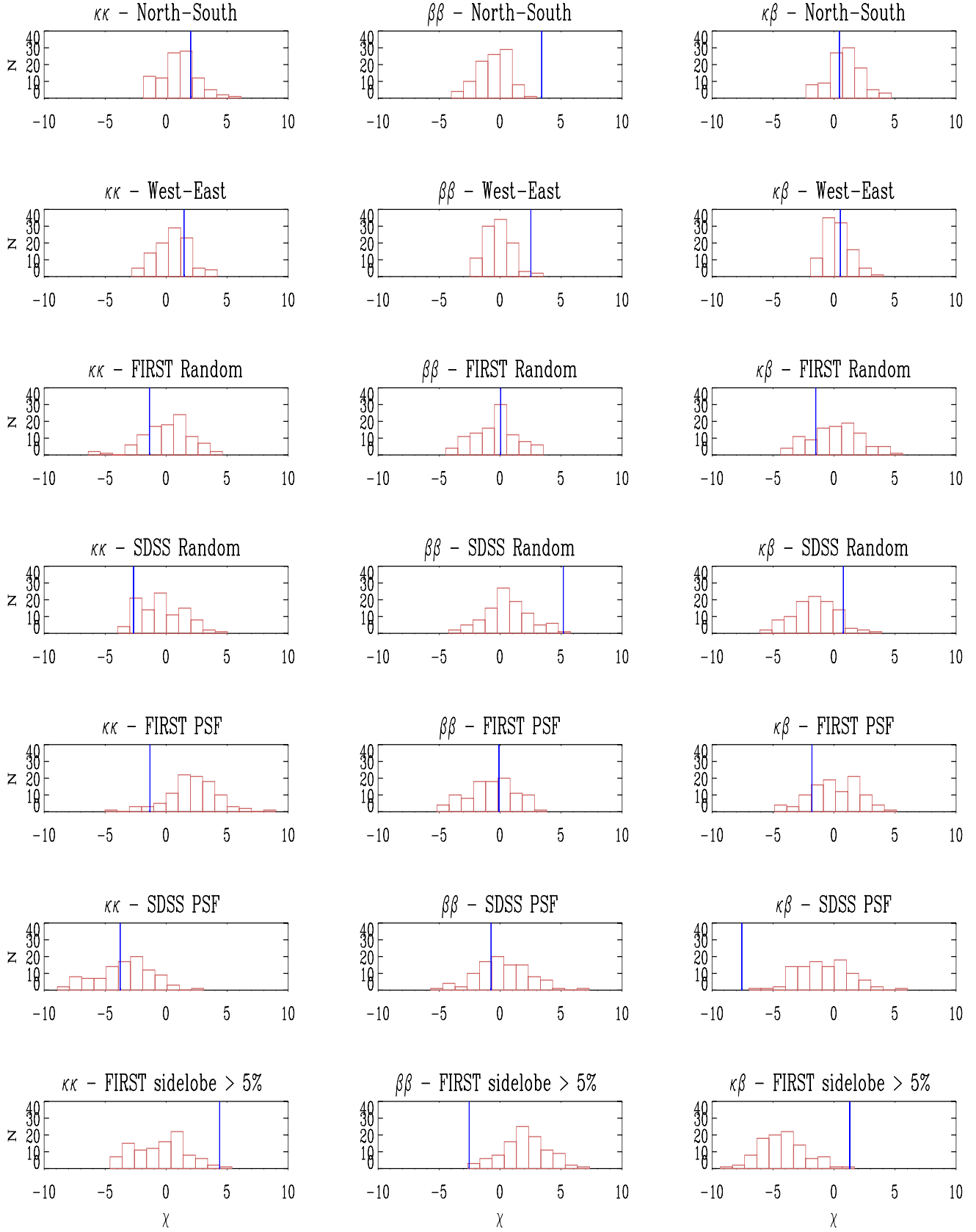


**Figure A2.** Histograms showing the distribution of  $\chi$  values (equation 41) measured from the simulations for the suite of null tests described in Section 6.2. The results are shown for the  $C_{\ell}^{\kappa\kappa}$  (left column),  $C_{\ell}^{\beta\beta}$  (centre column) and  $C_{\ell}^{\kappa\beta}$  (right column) power spectra. Over-plotted as the vertical blue line is the equivalent value for the real data measurement.